nature plants

ARTICLES

https://doi.org/10.1038/s41477-022-01145-7

Check for updates

A conformational switch in the SCF-D3/MAX2 ubiquitin ligase facilitates strigolactone signalling

Lior Tal, Malathy Palayam, Mily Ron, Aleczander Young, Anne Britt and Nitzan Shabek ✉

Strigolactones (SLs) are a class of plant hormones that regulate numerous processes of growth and development. SL perception and signal activation involves interaction between F-box E3 ubiquitin ligase D3/MAX2 and DWARF14 (D14) α/β-hydrolase in a SL-dependent manner and targeting of D53/SMXL6/7/8 transcriptional repressors (SMXLs) for proteasome-mediated degradation. D3/MAX2 has been shown to exist in multiple conformational states in which the C-terminal helix (CTH) undergoes a closed-to-open dynamics and regulates D14 binding and SL perception. Despite the multiple modes of D3–D14 interactions found in vitro, the residues that regulate the conformational switch of D3/MAX2 CTH in targeting D53/SMXLs and the subsequent effect on SL signalling remain unclear. Here we elucidate the functional dynamics of ASK1–D3/MAX2 in SL signalling by leveraging conformational switch mutants in vitro and in plants. We report the crystal structure of a dislodged CTH of the ASK1–D3 mutant and demonstrate that disruptions in CTH plasticity via either CRISPR–Cas9 genome editing or expression of point mutation mutants result in impairment of SL signalling. We show that the conformational switch in ASK1–D3/MAX2 CTH directly regulates ubiquitin-mediated protein degradation. A dislodged conformation involved in D53/SMXLs SL-dependent recruitment and ubiquitination and an engaged conformation are required for the release of polyubiquitinated D53/SMXLs and subsequently D14 for proteasomal degradation. Finally, we uncovered an organic acid metabolite that can directly trigger the D3/MAX2 CTH conformational switch. Our findings unravel a new regulatory function of a SKP1–CUL1–F-box ubiquitin ligase in plant signalling.

Strigolactones (SLs) are plant hormones that play an essential role in the regulation of various developmental processes including shoot branching and root architecture. SLs also act as rhizospheric-secreted signals facilitating communication with symbiotic fungi and parasitic plants[1–6]. The activation of several signalling cascades governed by plant hormones involves the action of E3 ubiquitin (Ub) ligase enzymes that coordinate specific targeting and degradation of transcriptional repressors[7]. Genetic and biochemical studies showed that SLs are perceived by the α/β-hydrolase receptor DWARF14 (D14)[8,9] that interacts with the E3 Ub ligase DWARF3/MORE AXILLARY BRANCHES2 (D3/MAX2)[2,10] to target DWARF53 (D53)/SUPPRESSOR OF MAX2-LIKE 6, -7 and -8 (SMXL6/7/8) by ubiquitination and subsequent degradation via the 26S proteasome[11–13]. D3/MAX2 is a leucine-rich repeat (LRR)-type F-box protein that binds *Arabidopsis* (At) SKP1-like protein (ASK1) to function as a substrate receptor of an SKP1–CUL1–F-box (SCF) Ub ligase complex[2]. D53/SMXLs proteins have weak similarity to AAA+ ATPase proteins, contain transcriptional repression EAR motifs, and are rapidly degraded following SL treatment[12–15]. About 400 SL-responsive genes were identified in an *Arabidopsis* transcriptome analysis following synthetic SL treatment, and SMXL6 was found to function as an autoregulator by directly binding SMXL6, SMXL7 and SMXL8 promoters[16].

Coupled with genetic findings, structural biology studies have deepened our understanding of signalling mechanisms for several plant hormones such as auxin (AUX) and jasmonate. These two hormones are directly perceived by their E3 ligases, TIR1 and COI1 respectively, and facilitate the interaction of the E3 ligase with its target protein (auxin/indole-3-acetic acid (AUX/IAA) or JASMONATE ZIM-DOMAIN (JAZ))[17–19]. In striking contrast, SL perception and signalling exhibit more complex non-binary interactions between the D14 hydrolase (the SL receptor), $SCF^{D3/MAX2}$ (the E3 ligase) and its target D53/SMXLs transcription co-repressors, providing opportunities for additional modes of regulation. Although the structure of the D14-SL–D3–D53 holocomplex remains to be determined, crystal structures of the individual components such as D14, D3 and ASK1–D3–D14 complex were recently determined and helped to shed light on SL perception and hydrolysis in the signalling cascade[20–22]. Despite these advances, many questions remain unanswered regarding the plasticity of D3/MAX2 in the recruitment of D14 and D53/SMXLs. Recent important attempts to decipher the SL-signalling mechanism were revealing and further substantiated the dynamic nature of the SL complex[21,22]. The crystal structure of rice ASK1–D3 with AtD14 captured the receptor in a distinct conformation suggesting a post hormone hydrolysis state or the presence of a covalently bound hydrolysis intermediate product in the D14-SL binding pocket[21]. In another structure, rice D14 was captured with SL in complex with the last LRR20 of D3, the C-terminal helix (CTH), presumably in a pre-hydrolysis state, as demonstrated by the ability of the CTH to inhibit SL hydrolysis by D14 (ref. [22]). Although the exact function and timing of SL hydrolysis within the signalling complex has been an active yet elusive subject of an increasing number of studies[21,23,24], recruitment and targeting of D53/SMXLs by D3/MAX2–D14 remain largely unexplored.

Notably, the crystal structures of ASK1–D3 revealed conformational dynamics with three distinct states that are centred on the D3-CTH region: an engaged/closed conformation, in which the CTH is arranged as a typical LRR α-helix and forms a complete LRR horseshoe shape; a flexible form, in which the CTH appears as a random coil; and a dislodged/opened form, in which the CTH is completely disordered or missing in the structure[22]. Collectively, the current molecular models of ASK1–D3–D14 denote distinct interfaces between D14 and D3, as well as potentially different SL hydrolysis states, thereby corroborating the dynamic rearrangement

Department of Plant Biology, College of Biological Sciences, University of California – Davis, Davis, CA, USA. ✉e-mail: nshabek@ucdavis.edu

upon signal perception and transduction. Despite the differences, both D3–D14 structures highlight the importance of CTH as part of the D3–D14 interface: in one crystal structure, D3-CTH is found in a dislodged conformation creating an interface with D14 mediated by the distal part of the CTH (for example, Glu700 and Leu707);[22] in the other crystal structure, D3-CTH is found completely engaged with additional residues interacting with D14, as well as with the proximal part of CTH (for example, Thr699, Arg702 and Ser705)[21]. Together, the molecular mechanisms of systemic SL-signalling activation and particularly the exact function of $SCF^{D3/MAX2}$ Ub ligase CTH dynamics in targeting SMXLs/D53 remain largely unexplored.

Notably, $SCF^{D3/MAX2}$ function is also implicated in the karrikin (KAR) signalling pathway together with the α/β-hydrolase receptor KARRIKIN INSENSITIVE2 (KAI2). It has been proposed that MAX2–KAI2 signalling complex can target SUPPRESSOR OF MAX2 1 (SMAX1) and SMXL2 upon perception of smoke-derived KAR molecules or by an as yet unidentified endogenous ligand[13,25–29].

Here we focus on SL signalling and reveal the biological relevance of altered conformations of $SCF^{D3/MAX2}$ Ub ligase and their impacts on D14-SL recruitment, D53/SMXLs ubiquitination and subsequent degradation. To that end, we systematically integrated structure–function, biochemical and genetic approaches to facilitate specific conformational changes in D3/MAX2 and test their functionality in vitro and in planta. We determined the crystal structure of CTH-dislodged ASK1–D3 mutant and generated multiple transgenic and CTH clustered regularly intespersed palindromic repeates (CRISPR)–CRISPR associated protein 9 (Cas9) genome-edited *Arabidopsis* lines, further revealing the molecular mechanism regulating systematic developmental outputs triggered by SL. Remarkably, structure–function analysis uncovered a highly reactive pocket within ASK1–D3/MAX2 that accommodates the evolutionarily conserved C terminus aspartic residue and can also be compromised by specific tricarboxylate natural metabolite. Altogether, we demonstrate that the switch between the different conformations of D3/MAX2 CTH is a key element in maintaining functional SL signalling in plants and that these dynamics can be triggered by a primary metabolite. Our findings add a new layer of regulation to phytohormone-governed processes and suggest a new paradigm in SCF Ub ligase-based regulatory modes.

Results

D720K switches D3-CTH from an engaged to dislodged state. To study the mode of action of D3-CTH conformations in plants, we first set out to generate a full-length ASK1–D3 with a dislodged CTH and test its structure and function. Inspection of the engaged form of the ASK1–D3 crystal structure positioned the evolutionarily conserved C terminus aspartic residue (D720 in rice D3, Fig. 1a) in a well-defined charged concave pocket, we termed the D-pocket. Interestingly, the D-pocket is clustered by highly conserved residues from both D3 (R36, H39, R40, R657 and R680) and the adaptor ASK1 (R152), forming a highly positive charged micro-environment (Fig. 1a). Thus, the CTH (LRR20) is trapped in an engaged state via D720 carboxyl groups that form tight salt-bridge bonds with R657, R40, R36 and R152 side chains. To perturb these polar interactions, we generated an ASK1–D3 mutant protein by replacing D720 with a lysine ($D3^{D720K}$, Fig. 1b). ASK1–D3 and ASK1–$D3^{D720K}$ proteins were designed as split constructs, as shown previously for ASK1–D3, to eliminate a long disordered loop for structure–function studies and to enable us to monitor with precision any changes within the C-terminal region (LRR14–20)[22]. The split constructs generate two domains, the N-terminal domain (NTD) and the C-terminal domain (CTD), both of which are naturally assembled with ASK1 and separated using SDS–polyacrylamide gel electrophoresis (SDS–PAGE; Supplementary Fig. 1a). The CTD of ASK1–$D3^{D720K}$ exhibits a slight shift on the gel, probably because of the alteration from D to K, as shown previously for other modified D3 (ref. [22]). Notably, when ASK1–D3 and ASK1–$D3^{D720K}$ were subjected to limited proteolytic digestion assays, the CTD of $D3^{D720K}$ was consumed completely after 5 min of incubation with trypsin, in contrast to the CTD of D3, which was still visible after 15 min of incubation (Fig. 1b and Source Data Fig. 1). Following additional validations with mass spectrometry (Supplementary Fig. 1b), these results suggests that $D3^{D720K}$ CTD is more susceptible to trypsin digestion, because ASK1–$D3^{D720K}$ CTH is likely to be trapped in a dislodged conformation. Comparative differential scanning fluorimetry (DSF) demonstrated that ASK1–$D3^{D720K}$ has a significant lower melting temperature (ΔTm ~10 °C) than ASK1–D3 (Fig. 1b), further supporting that D720K substitution is sufficient to switch the D3-CTH from a rigid engaged form to a flexible dislodged state.

To further assess $D3^{D720K}$, we determined the crystal structure of the ASK1–$D3^{D720K}$ complex at 3 Å (Fig. 1c and Supplementary Table 1). Similar to the previously reported structure of D3 with dislodged CTH[22], the structure of ASK1–$D3^{D720K}$ adopts a horseshoe-shaped solenoid compromised of 20 LRRs and an N-terminal F-box domain assembled with ASK1. Interestingly, LRR20 (the CTH) appeared to be completely disordered with an absence of defined electron density (ED), substantiating that ASK1–$D3^{D720K}$ is found in a CTH-dislodged state and/or completely disordered (Fig. 1c). Comparative structural analysis between the closed engaged state[22] and the structure reported here reveal a shift in LRR18 and LRR19 between the two forms, ASK1–D3 versus ASK–$D3^{D720K}$, with a root mean square deviation (r.m.s.d.) of 0.6 and 2.8 Å respectively (Fig. 1d). Here, the topological displacement of LRR19 in ASK–$D3^{D720K}$ could occur only in the absence of an engaged CTH, which otherwise would clash with LRR20 residues. To monitor ASK1–D3 conformational dynamics over time, we carried out comparative molecular dynamics simulations using a Martini coarse-grained force field[30,31]. Here, all atoms were plotted as a function of time for ASK1–D3 and ASK1–$D3^{D720K}$, as well as for the CTH region of ASK1–D3 and the modelled CTH of ASK1–$D3^{D720K}$ (Extended Data Fig. 1a). Indeed, the plasticity of the CTH region is significantly amplified in ASK1–$D3^{D720K}$ as evidenced by the r.m.s.d., root mean square fluctuation (r.m.s.f.) and conformational cluster analysis plot that deviated strongly between the two forms (~1 nm compared with ~0.5 nm in D3; Extended Data Fig. 1b). In summary, the ASK1–$D3^{D720K}$ mutant exhibits a dislodged CTH state and can be further leveraged to test its ability to recruit the SL receptor, D14. Remarkably, using a pull-down assay, glutathione S-transferase (GST)–D14 is able to bind either His-tagged ASK1–D3 or ASK1–$D3^{D720K}$ in the presence of the SL synthetic analogue, GR24 (Extended Data Fig. 1c). Using an SL fluorogenic hydrolysis assay, it has previously been shown that when ASK1–D3 recruits D14, the rate of SL hydrolysis is decreased[21]. Similarly, D14-SL hydrolysis is substantially decreased in the presence of ASK–$D3^{D720K}$ (Extended Data Fig. 1d), further demonstrating that D3 with dislodged CTH is able to recruit D14-SL. We next investigated the function of the dislodged CTH protein form in vivo using the *Arabidopsis* orthologue, MAX2.

The dislodged CTH state of *Arabidopsis* MAX2 inhibits SL signalling. To determine the function of $D3^{D720K}$ with dislodged CTH, we generated a similar mutant in *Arabidopsis* MAX2 (AtMAX2) by replacing the C terminus aspartic residue at position 693 with a lysine (D693K). *MAX2* is expressed ubiquitously throughout the plant and expression of *35S:MAX2* is sufficient to complement the mutant phenotypes[2]. We generated transgenic *Arabidopsis* lines expressing $MAX2^{D693K}$ under the control of the ubiquitin-10 promoter (*pUBQ*) in the *max2* loss-of-function genetic background[1]. Interestingly, whereas *max2*/*pUBQ:MAX2* complemented *max2* phenotypes, *max2*/*pUBQ:*$MAX2^{D693K}$ plants had a rosette leaf shape and increased branching similar to that of *max2* mutant plants (Extended Data Fig. 2a,b). Expression of *pUBQ:MAX2* in wild-type (WT) Col-0 background showed little to no effect (Fig. 2a) similar

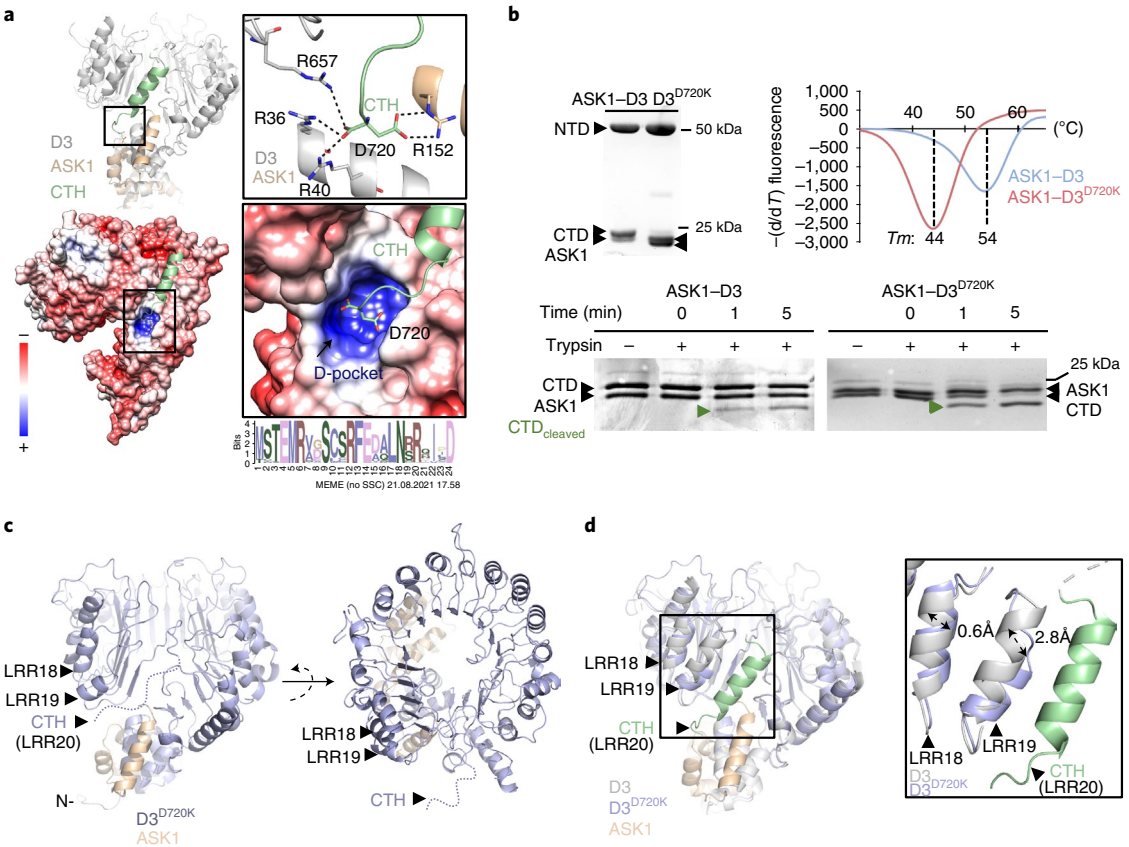

Fig. 1 | Structural and functional characterization of dislodged ASK1–D3-CTH. a, Overall structure of ASK1 (wheat) bound to D3 (grey) with its CTH (green) showing the D720 in stick representation and close-up view of D720 (aspartic residue) stabilized by interacting residues (top). Electrostatic surface representation of ASK1–D3 and close-up view of the D-pocket (blue, cluster of basic/positively charged residues) (bottom). A conservation logo plot is shown by the colour-coded bar graph representing the conservation of each position in the CTH sequence (analysed from 37 plant species). SSC, small sample correction. **b**, Side-by-side ASK1–D3 and ASK1–D3^{D720K} complexes from the size-exclusion chromatography peak fraction. Complexes were separated on SDS–PAGE followed by Coomassie staining. The three distinct bands correspond to the NTD of D3, CTD of D3 (CTD) and ASK1 (left). The melting temperature (*Tm*) of each protein complex is achieved by DSF (right). Limited proteolytic trypsin digestion is shown for ASK1–D3 and ASK1–D3^{D720K}, SDS–PAGE followed by Coomassie stain visualized the lower molecular mass cleavage products of CTD (CTD cleaved is denoted in green). Experiments were repeated independently three times with similar results. **c**, Overall view of ASK1 bound to D3^{D720K} crystal structure; front and top views of ASK1 (wheat) bound to D3^{D720K} (purple), LRR18–19 are denoted and the dislodged CTH is represented as dashed lines (LRR20). **d**, Superposition of ASK1–D3 (grey) and ASK1–D3^{D720K} (purple) showing the major changes (structural shifts) in LRR18–19 in proximity to LRR20 (CTH).

to that of previously reported *p35S:MAX2* lines[2]. However, plants expressing *pUBQ:MAX2^{D693K}* in a WT background exhibit various SL-signalling deficiency phenotypes in a dominant negative manner. Fifteen independently derived T1 transgenic lines were screened for each transgene and showed SL-signalling deficiency phenotypes (Supplementary Fig. 2a). Analyses were performed on representative homozygote T3 plant lines.

Young WT/*pUBQ:MAX2^{D693K}* plants grew compact rosettes with round leaves similar to the SL-signalling mutants, *max2* and *d14* (Fig. 2a). Following floral transition, *pUBQ:MAX2^{D693K}* plants released significantly more rosette axillary shoots than WT or WT/*pUBQ:MAX2*, but fewer than *max2* and *d14* (Fig. 2b). SL-signalling and biosynthesis mutants display delayed senescence phenotypes during dark incubation because SL biosynthesis is induced during and required for the efficient progression of leaf senescence[32,33]. Therefore, we tested the leaf senescence progression of detached leaves after dark incubation of both WT/*pUBQ:MAX2* and WT/*pUBQ:MAX2^{D693K}* plants. Leaves from WT/*pUBQ:MAX2^{D693K}* plants showed a significant delay in leaf senescence similar to that of *max2* and *d14* mutants. The WT/*pUBQ:MAX2* leaf senescence phenotype was similar to that of WT plants (Fig. 2c, left). Furthermore, following dark incubation, the chlorophyll content of WT/*pUBQ:MAX2* was similar to WT, but WT/*pUBQ:MAX2^{D693K}* plants show significantly higher chlorophyll content, similar to that of *max2* and *d14* mutants (Fig. 2c, right). These results demonstrate that WT/*pUBQ:MAX2^{D693K}* plants are compromised in SL signalling.

MAX2 is known to function in the light-mediated suppression of hypocotyl elongation and *max2* mutants exhibit long hypocotyls[2,34,13]. Therefore, we tested the effects of *MAX2^{D693K}* on hypocotyl elongation in seedlings grown under white light. WT/*pUBQ:MAX2^{D693K}* seedlings had longer hypocotyls than WT, but hypocotyl length in WT/*pUBQ:MAX2* was similar to WT (Fig. 2d). These results showed that the expression of *MAX2* in a dislodged CTH state, even in the presence of a WT copy of *MAX2*, inhibits SL signalling in a similar manner to the *max2* loss-of-function mutant, and highlight the regulatory role for MAX2 CTH conformation in facilitating SL signalling.

Perturbation of D-pocket in AtMAX2 inhibits SL signalling. Because the D720 of D3 resides in the D-pocket (Fig. 1a), we tested the effect on SL signalling by perturbing only the D-pocket. Inspection of ASK1–AtMAX2 modelled structure revealed key residues that are clustered to form the D-pocket in AtMAX2, similar to those in rice D3 (Fig. 3a). Using this model, we carried out

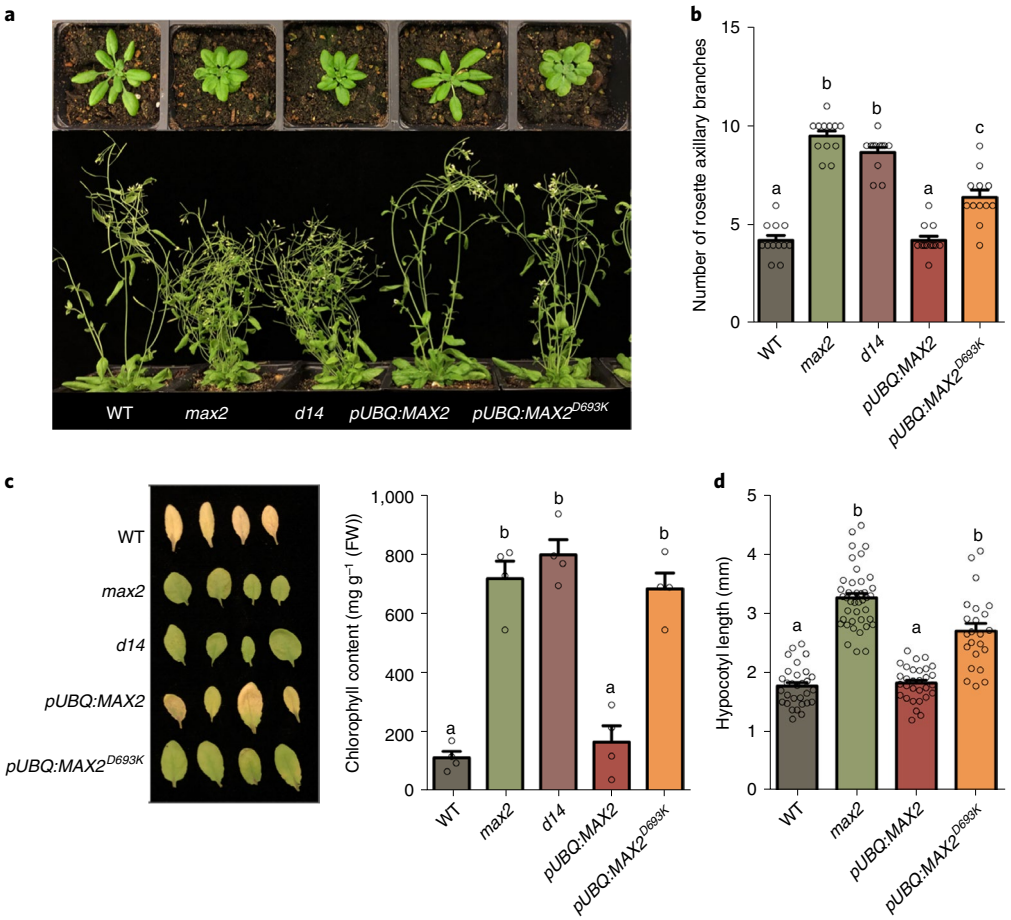

Fig. 2 | Functional characterization of dislodged ASK1–D3-CTH mutant in systemic SL signalling. a, Five-week-old plants exhibit SL-deficiency phenotypes that include changes in rosettes size and leaf shape (top). Eight-week-old plants show a SL-deficiency phenotype of increased branching (bottom). All transgenic plants are in a WT Col-0 background. **b**, Mean number of axillary rosettes branches (± s.e.m.). $n = 12$. One-way ANOVA and post hoc Tukey test, $P < 0.0001$. **c**, Detached rosette leaves following 7 days of dark incubation. Mean chlorophyll content (mg g^{-1}) of detached rosette leaves following dark incubation (± s.e.m.). $n = 4$. One-way ANOVA and post hoc Tukey test, $P < 0.0001$. FW, fresh weight. **d**, Mean length (mm) of hypocotyls of light-grown 10-day-old seedlings (± s.e.m.). WT, $n = 30$; *max2*, $n = 42$; *pUBQ:MAX2*, $n = 30$; and *pUBQ:MAX2*^{D693K}, $n = 23$. One-way ANOVA and post hoc Tukey test, $P < 0.0001$. **b**,**c**,**d**, Bars with the same letter are not significantly different; open circles represent data points.

mutational analysis to perturb the size of the D-pocket. We targeted the residues in positions R25 (inner part of the D-pocket) and S29 (outer part of the D-pocket) and generated a mutant containing R25F and S29F substitutions (MAX2^{R25F,S29F}). Structural analysis predicts that ASK1–MAX2^{R25F,S29F} will compromise the plasticity of the D-pocket by decreasing its size and disrupting the positioning of D693 in the pocket (Fig. 3a). To test the effect of the D-pocket, we generated a homozygous transgenic line of *pUBQ:MAX2*^{R25F,S29F} in a WT background. Fifteen independently derived T1 transgenic lines were screened and all demonstrated similar *max2* loss-of-function phenotypes in a dominant negative manner (Extended Data Fig. 3 and Supplementary Fig. 2b). WT/*pUBQ:MAX2*^{R25F,S29F} plants display increased branching (Fig. 3b and Extended Data Fig. 3) and delayed dark-induced leaf senescence compared with WT (Fig. 3c, left) but similar to *max2* and *d14*. The chlorophyll content of WT/*pUBQ:MAX2*^{R25F,S29F} plants was similar to that of *max2* and *d14* (Fig. 3c, right). Furthermore, under white light, WT/*pUBQ:MAX2*^{R25F,S29F} seedlings exhibit elongated hypocotyls similar to *max2* (Fig. 3d). Together, MAX2^{R25F,S29F} and MAX2^{D693K} represent variations of MAX2 that result in disruption of the engaged CTH form, and expression of either of the variants results in *max2* loss-of-function characteristic phenotypes.

CTH dynamics regulate Ub-mediated degradation of D53/SMXLs. Our results showed that in the presence of SL, D3/MAX2 with a dislodged CTH can recruit D14-SL (Fig. 1 and Extended Data Fig. 1). However, expression of D3/MAX2 with a dislodged CTH state results in loss of SL signal transduction in plants (Figs. 2 and 3). We therefore hypothesized that dislodged D3/MAX2 may interfere with the dynamics of ASK1–MAX2–D14-SL conformations and their ability to effectively target D53/SMXLs co-repressors to proteasomal degradation. Because the mode of interactions between SL-signalling components is largely elusive, it is unclear whether D53/SMXLs are recruited via D3/MAX2 in dislodged CTH form. We first tested the ability of ASK1–D3^{D720K} to recruit both D14 and D53 in an SL-dependent manner. We used the D2 domain of D53 ($D53_{D2}$) that has been shown to directly interact with D3–D14-SL[22,35–38] in a pulldown experiment and found that in the presence of D14-SL, His-tagged ASK1–D3 and ASK1–D3^{D720K} bind GST-tagged $D53_{D2}$ to a similar extent (Fig. 4a). Thus, the observed SL-signalling deficiency phenotypes of dislodged MAX2 CTH in *Arabidopsis* (Figs. 2 and 3) cannot be fully explained by a failure to recruit D53/SMXLs. These results raised an intriguing possibility that D53/SMXLs failed to be effectively degraded when bound by a dislodged D3/MAX2. To address this, we used plant cell-free ubiquitination assays to evaluate the Ub ligase

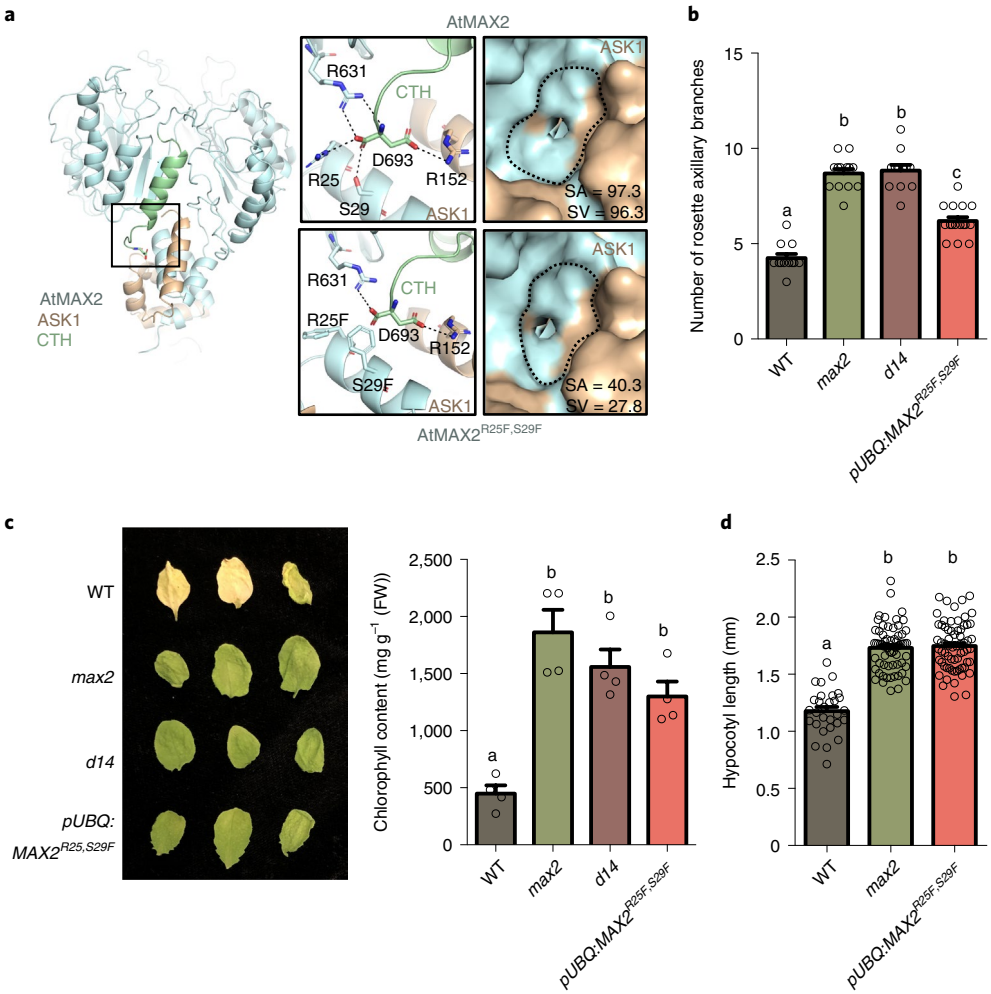

Fig. 3 | Functional characterization of D-pocket perturbed ASK1–D3 mutant in systemic SL signalling. a, Molecular structure model of *Arabidopsis* (At) ASK1–MAX2 displayed as cartoon representation (left) showing the D693 in sticks representation. ASK1 is coloured in wheat and AtMAX2 in cyan, CTH is in green. Close-up view of the stabilization or destabilization of the D693 interaction network within the D-pocket of AtMAX2 (top) and ASK1–AtMAX2^{R25F,S29F} (bottom), respectively. D-pocket topologies between the non-modified and modified (R25F, S29F) ASK1–AtMAX2 were analysed via CASTp; calculated surface area (SA) and surface volume (SV) values (Å^2 and Å^3, respectively) are shown (right). The dashed line indicates the altered circumference of the D-pocket compared with the mutant. **b**, Mean number of axillary rosettes branches (± s.e.m.). WT, $n=12$; *max2*, $n=13$; *d14*, $n=12$; and *pUBQ:MAX2*^{R25F,S29F}, $n=16$. One-way ANOVA and post hoc Tukey test, $P<0.01$. Transgenic plants are in WT Col-0 background. **c**, Detached rosette leaves following 7 days of dark incubation. Mean chlorophyll content (mg g^{-1}) of detached rosette leaves following dark incubation (± s.e.m.). $n=4$. One-way ANOVA and post hoc Tukey test, $P<0.01$. FW, fresh weight. **d**, Mean length (mm) of hypocotyls of light-grown 10-day-old seedlings (± s.e.m.). WT, $n=29$; *max2*, $n=65$; and *pUBQ:MAX2*^{R25F,S29F}, $n=66$. One-way ANOVA and post hoc Tukey test, $P<0.0001$. **b**,**c**,**d**, Bars with the same letter are not significantly different; open circles represent data points.

activities of ASK1–D3 and ASK1–D3^{D720K}. Polyubiquitination levels of D53$_{D2}$ were quantified by anti-Ub antibody following D53$_{D2}$ GST-pulldown in the presence of *Arabidopsis max2* cell extract supplemented with proteasome inhibitor, MG132, GR24, with or without recombinant ASK1–His-D3 or ASK1–His-D3^{D720K}, and D14. Interestingly, the levels of polyubiquitinated D53$_{D2}$ were significantly higher in the presence of the D3^{D720K} compared with D3 (Fig. 4b and Extended Data Fig. 4a). These findings further corroborate the ability of D3^{D720K} to specifically recruit D53$_{D2}$ but also suggest that it is the MAX2/D3 CTH-dislodged state that potentiates D53/SMXLs ubiquitination and proteasomal degradation. To test the latter, we employed a plant cell-free proteasomal degradation assay and monitored AtSMXL7$_{D2}$ levels (SMXL7 served as SMXLs representative in our experiments) in WT, *max2* and transgenic *pUBQ:MAX2*^{D693K} cell extracts. Remarkably, degradation of SMXL7$_{D2}$ was slow in the presence of *pUBQ:MAX2*^{D693K} cell extract (31% of proteins remaining after 80 min of incubation) compared with WT cell extract (16% of proteins remaining after 80 min of incubation), and it is significantly blocked in *max2* extract (Fig. 4c and Extended Data Fig. 4b).

It has been shown previously that MAX2/D3 also plays a role in SL-dependent proteasomal degradation of D14 in *Arabidopsis*[39] as well as in rice[40] following D53 degradation as a feedback mechanism for SL perception. To further elucidate the regulatory function of the MAX2/D3 CTH conformational switch, we tested the levels of *Arabidopsis* D14 in WT, *max2* and *pUBQ:MAX2*^{D693K} cell extract backgrounds. In agreement with SMXL7$_{D2}$ levels (Fig. 4c), D14 levels were higher in *pUBQ:MAX2*^{D693K} and *max2* extracts, compared with WT extracts (Fig. 4d). These results indicate that D53/SMXLs SL-dependent recruitment, ubiquitination and degradation are distinct processes modulated by D3/MAX2 CTH dynamics.

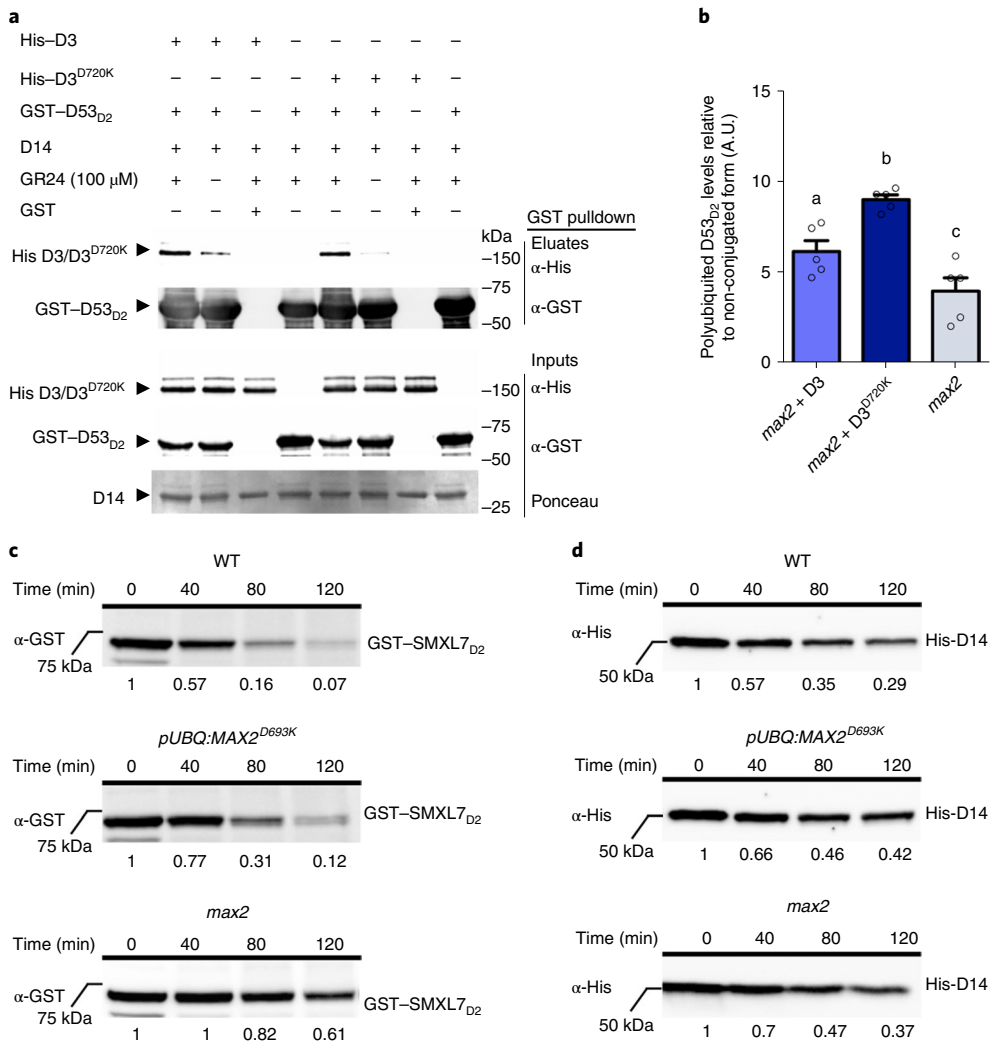

Fig. 4 | CTH dynamics affect D53/SMXL7 ubiquitin-mediated degradation by the Ub ligase D3/MAX2. a, GST-pulldown of GST–$D53_{D2}$, D14 and ASK1-His-D3 or ASK1-His-$D3^{D720K}$ in the presence or absence of GR24. Proteins were resolved by SDS–PAGE and were visualized via western blot analysis with anti-His and anti-GST antibodies, as indicated. **b**, Mean values of five experiment replicas measuring $D53_{D2}$ polyubiquitinated levels relative to its non-conjugated form (± s.e.m.) in the presence of *max2* total cell extract supplemented with recombinant ASK1-D3 or ASK1-$D3^{D720K}$, as indicated. A.U., arbitrary units. One-way ANOVA and post hoc Tukey test, $P < 0.05$. Bars with different letters are significantly different; open circles represent data points. **c**,**d**, Degradation assays using WT (top), *pUB: MAX2*^{D693K} (middle) and *max2* (bottom) total cell extracts monitoring GST-$SMXL7_{D2}$ (**c**) or His-D14 (**d**) at the indicated time points (numbers under the blots are the proportions of protein remaining that were quantified and compared with $T = 0$). All proteins were resolved by SDS–PAGE and analysed by western blot using anti-GST or anti-His antibodies. All experiments were repeated three to five times.

D3/MAX2 conformational switch is triggered by citrate. Our structural data combined with biochemical assays and transgenic plant analysis demonstrate that the functions of $SCF^{D3/MAX2}$ Ub ligase in SL signalling are regulated by a conformational switch between the engaged and dislodged CTH states. Previous studies on Ub ligases in plant signalling pathways have shown the critical involvements of small-molecule metabolites in regulating target substrate recruitment such as inositol phosphates (InsPs) in COI1–JAZ and TIR1–AUX/IAA complexes[18,19]. These metabolites were initially discovered by inspecting the crystallographic data of the macromolecule structures. Inspired by this, we carried out a thorough examination of our X-ray crystallography data. Strikingly, the dislodged ASK1–$D3^{D720K}$ crystal structure revealed the presence of a clear, yet unmodelled blob of ED positioned in and occupying the D-pocket shown in the difference Fourier map (Fig. 5a). Interestingly, when inspecting the ED of the dislodged form of ASK1–D3 (PDB: 6BRO)[22], a similar ED is revealed. In both cases, the unmodelled ED appears to form additional contacts within the D-pocket compared with the D720 residue, suggesting a trapped aspartic-like moiety. Although the source of this molecule is unknown, it has been shown that co-factors and metabolites can be either co-purified and/or co-crystallize with the proteins[18,19]. Further interrogation of our specific crystallization conditions identified a mixture of organic acids. It is therefore possible that a small molecule with similar carboxylate groups will be able to out-compete D720 and trigger the conformational switch.

To address this, we subjected ASK1–D3 to limited proteolytic digestion in the presence of a variety of tricarboxylic acid cycle metabolites. Here, identical concentrations of different organic acids were incubated with ASK1–D3 under the same conditions (pH 6) for 15 min with trypsin. Remarkably, ASK1–D3 CTH was in a dislodged state in the presence of citrate, as exemplified by the increased susceptibility of the CTD to digestion (Fig. 5b). Furthermore, comparative analysis by titration of either succinate (dicarboxylate) or citrate (tricarboxylate) under the same trypsin-limited proteolysis conditions had a drastic effect on the

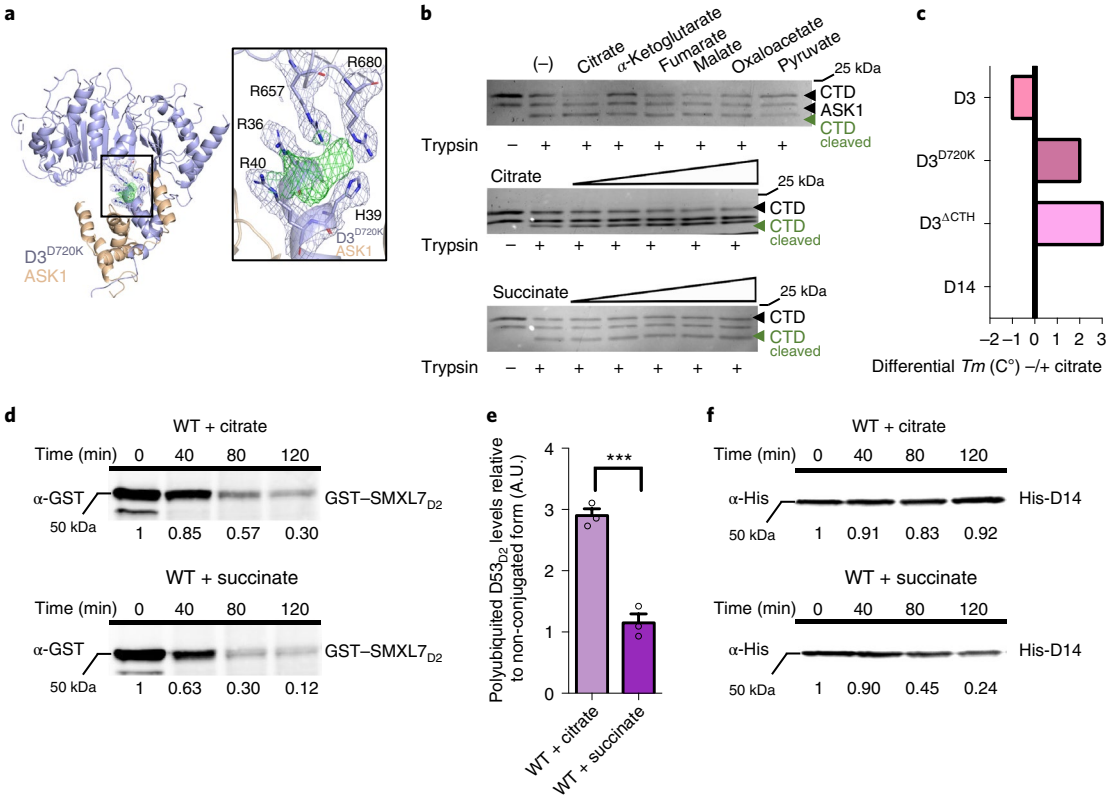

Fig. 5 | Structure–function analysis of ASK1–D3-citrate complex dynamics. a, Inspection of ASK1–D3^{D720K} crystal structure and an unmodelled ED blob (green) trapped in the D-pocket is shown by an $F_o - F_c$ map (3.0σ). Close-up view of the $F_o - F_c$ (3σ) and $2F_o - F_c$ map (1.0σ) of the unmodelled blob (green) and the interacting residues in the D-pocket of ASK1–D3^{D720K}. **b**, Limited proteolytic trypsin digestion is shown for ASK1–D3 in the presence of the indicated organic acids (top), and in the presence of increasing concentrations of citrate or succinate (middle and bottom, respectively). SDS–PAGE followed by Coomassie stain visualized lower molecular mass cleavage products of CTD (CTD cleaved is denoted in green). The experiment was repeated independently three times with similar results. **c**, DSF analysis of ASK1–D3, ASK1–D3^{D720K}, ASK1–D3$^{\Delta CTH}$ and D14, are represented as the shift in protein melting temperature (Δ*Tm*) of samples with and without citrate treatment. All experiments were performed in triplicate. **d**, Degradation of GST–SMXL7$_{D2}$ in the presence of WT total plant cell extract at the indicated time points (numbers under the blots are the proportions of protein remaining that were quantified and compared with $T = 0$) and supplemented with citrate or succinate. **e**, Mean values of three experiment replicates measuring polyubiquitinated D53$_{D2}$ levels in WT plant cell extract relative to its non-conjugated form in the presence of citrate or succinate (± s.e.m.). Two-tailed Student's *t*-test, $P = 0.0007$. **f**, Degradation of His-D14 in the presence of citrate or succinate. All experiments were repeated three times. Proteins in **e** and **g** were resolved by SDS–PAGE and detected using western blot analysis with the indicated antibodies.

CTD in the presence of citrate compared with no effect in the presence of succinate. Notably, our SL fluorogenic hydrolysis assays exhibited a decrease in the rate of SL hydrolysis by D14 in the presence of ASK–D3 and citrate compared with succinate, suggesting that ASK1–D3–citrate favoured the dislodged conformation. In the same experiment, ASK–D3^{D720K} inhibited D14-SL hydrolysis to a similar extent as ASK1–D3–citrate, but was not affected by either citrate or succinate (Extended Data Fig. 5a), further corroborating that citrate triggered the ASK1–D3 dislodged state. We further examined the ASK1–D3–citrate interaction using DSF and detected a thermal shift in the presence of citrate (Fig. 5c). Interestingly, citrate triggered an increase in *ΔTm* for both ASK1–D3^{D720K} and ASK1–D3$^{\Delta CTH}$ that completely lacks the CTH[22], probably because of the added accessibility of citrate to the D-pocket in these mutants (Fig. 5c). As a control, D14 showed no changes in protein stability or its activity in the presence of either citrate or succinate. Furthermore, our in silico molecular docking analysis identified citrate as the best fit to accommodate the ED in comparison with all other molecules in the crystallization condition (Extended Data Fig. 5b). Fitting anion-rich citrate (three carboxylate anionic groups) compared with the C terminus aspartic residue (with two carboxylate groups) of ASK1–D3 within the positively charged D-pocket further rationalized the ability of this metabolite to trigger a conformational switch. In the ASK1–D3^{D720K}–citrate complex, the O5 and O6 atoms of citrate replace the aspartate terminal carboxyl and its oxygen atoms, and the O3 and O4 atoms mimic the OD1 and OD2 atoms (side chains) of aspartate (Extended Data Fig. 5b). The O5 and O6 atoms of the citrate moiety form a strong hydrogen bond interaction with the NH2 atoms of R40 and R36 (distance of 2.7 and 3.2 Å respectively) and are stabilized by Van der Waals interactions with other basic residues such as R625, R648 and H39.

To test the impact of citrate on SL signalling, we monitored D53$_{D2}$/SMXL7$_{D2}$ ubiquitination and degradation in a plant cell-free system with addition of citrate or succinate as a control. In agreement with our previous protein degradation results, using *pUBQ:MAX2^{D693K}* cell extract (Fig. 4c), SMXL7$_{D2}$ levels were almost twice as high in the presence of citrate compared with succinate after 80 min of incubation in WT cell extract (Fig. 5d). In addition, the polyubiquitination levels of D53$_{D2}$ were higher in the presence of citrate (Fig. 5e and Extended Data Fig. 5c) and similar to levels observed for the His-D3^{D720K} dislodged CTH form (Fig. 4b). Furthermore, proteasomal degradation of D14 was slowed in the presence of citrate but not succinate in a WT background (Fig. 5f).

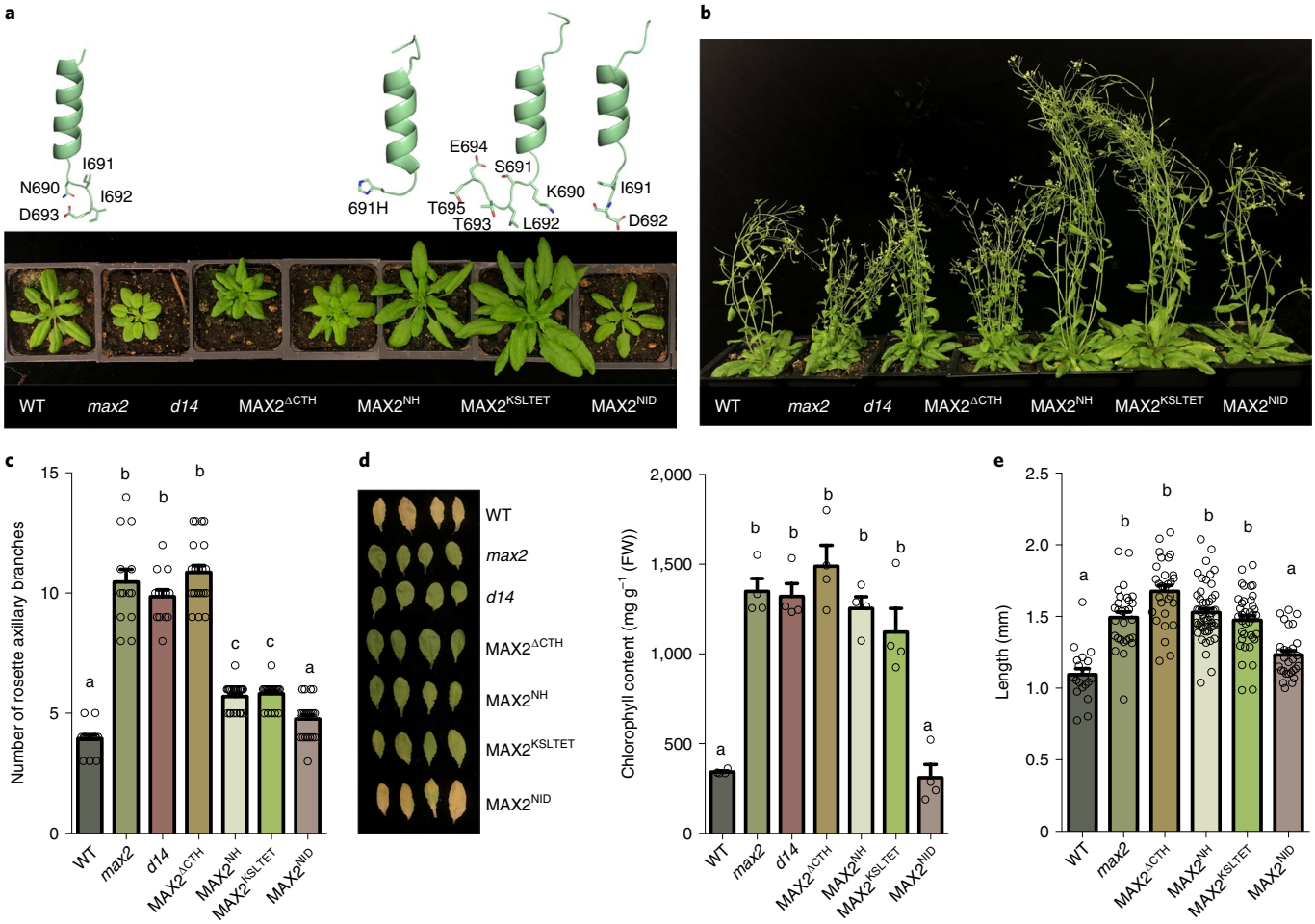

Fig. 6 | CRISPR–Cas9-guided mutagenesis of CTH of MAX2 results in SL-signalling deficiency phenotypes. a, Five-week-old CRISPR–Cas9 genome-edited plants with changes in rosettes size and leaf shape. Plants are in a WT Col-0 background. CTH-predicted structural modifications produced by CRISPR–Cas9 are shown in the top panel. **b**, Eight-week-old CRISPR–Cas9 genome-edited plants exhibit the SL-deficiency phenotype of increased branching. **c**, Mean number of axillary rosettes branches (± s.e.m.). WT, $n=15$; *max2*, $n=11$; *d14*, $n=9$; MAX2$^{\Delta CTH}$, $n=21$; MAX2^{NH}, $n=23$; MAX2^{KSLTET}, $n=21$; and MAX2^{NID}, $n=21$. One-way ANOVA and post hoc Tukey test, $P<0.05$. **d**, Detached rosette leaves following 7 days of dark incubation. Mean chlorophyll content (mg g^{-1}) of detached rosette leaves following dark incubation (± s.e.m.). $n=4$. One-way ANOVA and post hoc Tukey test, $P<0.0001$. FW, fresh weight. **e**, Mean hypocotyl length (mm) of light-grown 10-day-old seedlings (± s.e.m.). WT, $n=19$; *max2*, $n=29$; MAX2$^{\Delta CTH}$, $n=29$; MAX2^{NH}, $n=50$; MAX2^{KSLTET}, $n=38$; and MAX2^{NID}, $n=29$. One-way ANOVA and post hoc Tukey test, $P<0.05$. **c**,**d**,**e**, Bars with the same letter are not significantly different; open circles represent data points.

To verify the specific effects of citrate on SMXL7$_{D2}$ degradation and overrule any non-specific effects of citrate on proteasomal degradation, we tested the levels of AUX/IAA7$_{D2}$ with citrate or succinate and observed no significant differences (Extended Data Fig. 5d). Together, these findings indicate that citrate or a citrate-like organic acid triggers an ASK1–D3/MAX2 conformational switch by occupying the D-pocket and as a result, either competes off the C terminus aspartic residue or prevents the dislodged CTH from folding back into an engaged conformation.

Genome-edited MAX2-CTH variants compromise SL signalling. To generate MAX2 variant with a dislodged CTH in *Arabidopsis*, we employed a CRISPR–Cas9 approach and designed single guide RNAs that recognize regions spanning the MAX2-CTH. Two guide RNAs were designed and cloned separately, employing a protospacer adjacent motif (PAM) recognition sequence at the end of *MAX2*, utilizing either CAS9 or CAS9VQR[41] (Extended Data Fig. 6a). We screened and identified T3 homozygous transgenic lines free of the Cas9 transgene with short chromosomal deletions in *MAX2*. We termed these genome-edited mutant lines, expressing different MAX2 variants, according to the detected changes in the MAX2 sequence. These include complete deletion of the CTH region (MAX2$^{\Delta CTH}$); replacement of the three C-terminal residues I691, I692, D693 with a single histidine (MAX2^{NH}); replacement of four C-terminal residues N690, I691, I692, D693 with KSLTET (MAX2^{KSLTET}); and deletion of I692 (MAX2^{NID}) (Extended Data Fig. 6a). Five-week-old MAX2$^{\Delta CTH}$ plants showed compact rosette and rounded leaves similar to that of *max2* and *d14* mutants. By contrast, MAX2^{NH} and MAX2^{KSLTET} lines showed rosette leaves with increased blade length and width compared with the WT control (Fig. 6a and Extended Data Fig. 6b). Furthermore, following bolting, the primary floral stem of MAX2^{NH} and MAX2^{KSLTET} lines were thicker than WT (Extended Data Fig. 6c). MAX2^{NID} showed little developmental difference compared with WT (Fig. 6b).

We quantified plant branching by counting the number of axillary rosette shoots in these mutants. Whereas MAX2$^{\Delta CTH}$ lines exhibit similar increased branching to the loss-of-function SL-signalling mutants, MAX2^{NH} and MAX2^{KSLTET} display a minor increase in branching and MAX2^{NID} shows no increased branching phenotype (Fig. 6c). We next measured detached leaf chlorophyll

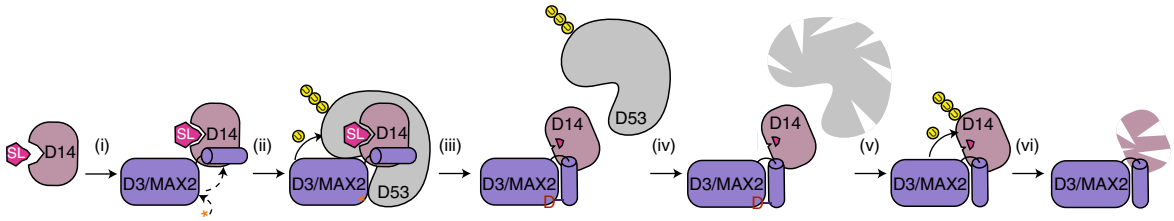

Fig. 7 | An updated model for SL signalling. Following SL (pink) perception by D14 (blush) (i), D3/MAX2 (purple) with dislodged CTH, that can be triggered by citrate (denoted by an orange asterisk), binds D14 (ii). D3/MAX2–D14–SL recruits the co-repressor D53/SMXLs (grey) and subsequently mediates polyubiquitination (in yellow) (iii). Additional intramolecular topological changes within D14 (upon SL hydrolysis, the pink triangle represents a covalent intermediate molecule) and D3/MAX2 where the CTH is now closed/engaged (C terminus aspartate is repositioned in the D-pocket), allow the release of D53/SMXLs to the proteasome and removal of SL-responsive genes transcriptional repression (iv). Following the removal of D53/SMXLs, D14 becomes accessible to further ubiquitination (v) and subsequent proteasomal degradation enabling feedback regulation of the signalling cascade (vi).

content (mg g^{-1}) following dark incubation for all variant lines. Like SL-signalling mutants *max2* and *d14*, $MAX2^{\Delta CTH}$, $MAX2^{NH}$ and $MAX2^{KSLTET}$ show a delay in leaf senescence compared with WT and $MAX2^{NID}$ (Fig. 6d). When we compared hypocotyl length for seedlings grown under white light, we found that all structure-guided genome-edited lines except $MAX2^{NID}$ had significantly longer hypocotyls than WT (Fig. 6e). Together, our genome-edited *Arabidopsis* lines strengthen in vitro and crystallography findings that place the CTH at the interface between MAX2/D3 and D14-SL[21,22]. By fully removing the CTH, complete loss of SL signalling is achieved. Importantly, we show that amino acid alterations at the C terminus of the MAX2-CTH led to rosette branching, primary floral stem thickness and leaf morphology-related phenotypes in agreement with previously reported effects of non-degradable SMXL7 expression[15].

Discussion

The plasticity of D3/MAX2 LRR-F-box at its highly conserved C-terminal LRR19–20 region and particularly the last CTH have been suggested to play essential roles in the recruitment of D14 and D53/SMXLs in vitro[21,22]. The non-canonical SL perception and hydrolysis by D14 and the subsequent ubiquitination and proteasomal degradation of D14, add another layer of complexity to the cascade of events from initial stimuli to response at the protein and physiological levels. To the best of our knowledge, this work is the first to address these complexities by dissecting the role of D3/MAX2-CTH dynamics in SL signalling both in vitro and in planta. We demonstrate the structural and biochemical characteristics of dislodged/engaged (open/closed) dynamics that are mainly driven by the evolutionarily conserved aspartic C terminus residue (D720 in rice, D693 in *Arabidopsis*) forming a cluster of electrostatic interactions in a conserved D-pocket. Notably, for one of the previously published structures of ASK1–D3 with fully engaged CTH, the aspartic residue D720 was completely absent[21]. This is possibly due to differences in the pH of the crystallization conditions compared with the neutral pH in which the D720 is trapped in the D-pocket[22].

In this study, we generated an open conformation of D3/MAX2 in which the CTH remains dislodged (ASK1–$D3^{D720K}$ and $MAX2^{D693K}$). We cannot determine precisely the various possible CTH structural conformations when it is dislodged, given the limitations of molecular dynamics simulations that may not accurately predict the amino acid-specific secondary structure propensities[42]. Nevertheless, the crystal structure of the ASK1–$D3^{D720K}$ complex reported here, together with our systematic and comparative biochemical analysis of dislodged/engaged states, enabled us to further examine the impact of these dynamics on the SL-signalling complex both in vitro and in vivo.

We found that a dislodged CTH mutant ($D3^{D720K}$ or $MAX2^{D693K}$) can recruit D14 and D53/SMXLs to a similar extent as the WT protein, which typically exhibits both opened and closed forms. In *Arabidopsis*, *pUB:*$MAX2^{D693K}$ transgenic lines display SL-signalling deficiency phenotypes like *max2* and *d14*, compared with *pUB:MAX2*, in a dominant negative manner. Similar effects of both hemi- and homozygosity were reported previously for the expression of non-degradable SMXL7 (ref. [15]), thus *pUB:*$MAX2^{D693K}$ phenotypes are probably the result of a failure to efficiently degrade the SMXLs co-repressors. The observation that D53 undergoes hyper-polyubiquitination by ASK1–$D3^{D720K}$ strongly suggests that the dislodged CTH state potentiates substrate recruitment (with D14-SL) and mediates its ubiquitination but lacks the flexibility to fully promote its proteasomal degradation.

The importance of Ub ligases' modularity to effectively target their substrates has been shown in several studies[43–47]. Although these studies explain the intramolecular topological conformations that help position the E2 (Ub carrier enzyme) closer to its substrate, our model proposes that topological changes within single protein components may be required for effective substrate release post ubiquitination. Here, we propose that the CTH within the $SCF^{D3/MAX2}$–D14-SL–SMXLs complex folds back into its engaged state allowing the release of SMXLs/D53 and eventually D14 degradation (Fig. 7). This model remains oversimplified because of the many unknowns in this intricate assembly pathway. These include the conformational changes that D14 undergoes during or after the relatively slow hydrolysis of SL[21,23] while simultaneously recruiting SMXLs. Therefore, the precise interplay between those three signalling components remains to be addressed in future structural studies.

In this work, we quantified plant phenotypes resulting from changes in SL-regulated developmental processes to assess D3/MAX2 protein function. Yet, under white light, both SL and KAR/KAI2 ligand (KL) can influence hypocotyl length through the independent regulation of SMXL2 degradation[28,29]. Further research is needed to explore the specific effect of $SCF^{D3/MAX2}$ dynamics on the KAR/KL signalling cascade.

In addition to these findings, our biochemical and crystallographic data further reveal citrate as a ligand that can potentially bind the D-pocket, displacing D720 and triggering the D3/MAX2 conformational switch. Notably, the citrate–D-pocket cluster of interactions resembles the mode of citrate binding within citrate synthase where the citrate moiety is completely stabilized by basic residues[48]. Our SL hydrolysis data (Yoshimulactone Green (YLG) assays) show augmented inhibition of SL hydrolysis by D14–D3 when treated with citrate concentrations as low as 50 μM. Interestingly citrate treatment mimicked the inhibition of SL hydrolysis by D14–$D3^{D720K}$, corroborating that citrate not only triggers the

D3-CTH-dislodged state, but also facilitates the spatial arrangement of the D14–D3 complex during SL perception and hydrolysis.

The concept of metabolites as critical co-factors in regulating substrate recruitment by F-box LRR Ub ligase in plant signalling has previously been shown for COI1–JAZ (inositol pentakisphosphate)[19] and TIR1–AUX/IAA (inositol hexakisphophate)[18] that were co-purified and similarly identified by differential ED map inspections. It is compelling to place D3/MAX2 in a similar mode of regulation; however, unlike TIR1 and COI1 where InsPs directly coordinate the hormone and substrate bindings, here citrate allosterically promotes a conformational switch to regulate SL receptor and substrate recruitment. Biochemically, it is not surprising that an aspartic-like molecule containing carboxylate groups will be trapped in the pocket, yet it is intriguing that compared with other carboxylates tested, citrate was the most effective molecule. Like COI1/TIR1–InsPs profiling, our mass spectrometry analysis was unable to achieve the direct mass of citrate or organic acid-like molecules bound to the protein. The detection and biochemical analysis of many protein–metabolite interactions is challenging, particularly when certain metabolites such as D3–citrate naturally exhibit weak interactions (mM concentrations)[49,50]. This is exemplified by the relatively weak binding constants (K_m) of enzymes with their substrates, where the natural substrate is a metabolite (for example, the K_m values of citrate as a substrate of aconitate hydratase and citrate lyase are only 3 mM and 0.16 mM respecitvely[51]). Moreover, in the case of D3/MAX2, citrate does not serve as an enzyme substrate, but rather as an allosteric ligand with relatively weak binding affinity (low mM range) that is probably influenced by intercellular citrate levels. The dynamic flux of metabolite cellular concentrations, in particularly citrate, can be relatively high (ranging from 0.25 to 50 mM)[51–54] stimulated by environmental cues either through transport[55] or an increase in production[56]. In addition, citrate is dynamically distributed in all subcellular compartments[54,57,58]. The link between endogenous SL allocations, phosphate-poor soils and the overproduction of citrate in abiotic stress has been suggested in several studies in the past decade[59–63]. Interestingly, an early report found that SL stimulates the activation of mitochondria, a citrate production source, in arbuscular mycorrhizal fungi as part of fungi–root symbiosis[64,65]. Our study proposes a novel mechanistic link between organic acid flux and highly specific regulation of $SCF^{D3/MAX2}$ conformation by finetuning time-dependent ubiquitination and degradation of SMXLs/D53 and the SL-signalling response. Further studies in this direction are important to clarify the relationship of citrate or similar organic acid metabolite(s) to SL-signalling cascades and distinguish their regulatory function(s) in specific tissues, in symbiosis communication, and their structure–function impact on the signalling complex. Also, the possible impact of organic acid metabolite(s) on $SCF^{D3/MAX2}$ dynamics in KAR/KL signalling remains to be studied.

Lastly, our structure-guided genome-editing approach resulted in the generation of both strong and weak SL-signalling deficiency mutants lines. $MAX2^{\Delta CTH}$ plants are indistinguishable from *max2-2* loss-of-function plants and further corroborate the role of CTH in SL signalling by recruiting D14-SL and SMXLs, as shown in vitro in this study and previously[22]. In addition, our weak enhanced-branching mutants $MAX2^{NH}$ and $MAX2^{KSLTET}$ display an increase (over WT) in leaf blade size. These results are in agreement with previously reported studies showing that the expression of non-degradable $_{D}$SMXL6, $SMXL6^{\Delta P\text{-}loop}$ or $SMXL7^{\Delta P\text{-}loop}$ mutants in a WT background leads to the formation of a wider leaf blade[14,15,33]. Also, $SMXL7^{\Delta P\text{-}loop}$ plants exhibit gain-of-function effects when expressed in a *max2* background, indicating that an increase in SMXL7 activity results in a wider phenotypic array than the range between WT and loss-of-function mutants[15]. Although the precise MAX2-CTH conformational state in the CRISPR–Cas9-edited lines remains to be further studied, the $MAX2^{NH}$ and $MAX2^{KSLTET}$ leaf-shape phenotype probably stems from a decrease in targeted degradation of SMXLs. Both SL and KL signalling are involved in the regulation of leaf morphology[13,16,33]. Notably, *kai2* plants also showed longer and wider leaf blades to a similar extent as $MAX2^{NH}$ and $MAX2^{KSLTET}$, indicating that in addition to disruption in SL signalling, these mutant lines possibly show KL signalling deficiencies. Interestingly, structural simulation of ASK1–$MAX2^{NH}$ and ASK1–$MAX2^{KSLTET}$ positions the CTH in an engaged state by forming a new salt bridge with ASK1 (Extended Data Fig. 6d,e). The lines generated in this work provide new genetic tools to further investigate MAX2 involvement in SL signalling through the regulation of SMXLs, as well as in other signalling cascades and various developmental processes. Further investigation into the transcriptional landscape of these mutants may reveal novel MAX2 functions and provide insight into the role of CTH dynamics in regulating plant development.

Methods

CTH sequence conservation analysis. BLAST analysis and protein sequencing of D3/MAX2 CTH between orthologues were performed using the Plaza 3.0 project[66]. Analysis of CTH residues conserved between D3/MAX2 orthologues ($n = 37$) was performed using the MEME suite v.4.11.1 bioinformatics online tool[67].

Recombinant DNA techniques and plasmid construction. Amplification of DNA fragments was carried out using Phusion DNA polymerase (ThermoFisher Scientific). *Arabidopsis thaliana* complementary DNA served as the PCR template for the cloning of AtMAX2. The *Arabidopsis* UBQ10 promotor[68] was amplified from a pMOA series plasmid and cloned into the BJ36 vector using NdeI and SpeI sites. AtMAX2 was cloned using XmaI and BamHI sites. To obtain $AtMAX2^{D693K}$ and $AtMAX2^{R25E,S29F}$ site-directed mutagenesis was carried out using the restriction-free cloning protocol[69]. All constructs were subcloned into pART27 binary vector[70] and introduced into *Agrobacterium tumefaciens* strain GV3101 by electroporation.

For CRISPR–Cas9 cloning, we identified two targets in the end of *MAX2*. One guide with NGA PAM (*MAX2*_gRNA1) and one guide with NGG PAM (*MAX2*_gRNA2). Cloning into pEn-Chimera was performed according to the Gateway cloning protocol[71]. Two 23 bp overlapping oligos were annealed and cloned into BpiI-digested pEn-Chimera. The resulting plasmid was used in an LR recombination (ThermoFisher Scientific) to transfer the AtU6-26p-MAX2_-sgRNA cassette into a pMR396 binary vector containing AtRPS5Ap-SpCas9 and AtOLEp-AtOLE1-Citrine or into pMR481, in which the Cas9 in pMR396 was replaced with SpCas9(VQR)[72] to generate pMR691(gRNA2) and pMR689(gRNA1) respectively[73]. Binary vectors were introduced into *Agrobacterium tumefaciens* strain GV3101 by electroporation.

Plant growth conditions and transgenic lines selection. Mutant seeds of *A. thaliana* (Col-0 background) were obtained from the Arabidopsis Biological Research Center (ABRC), including the CS956 for *max2-2* (AT2G42620) mutant line and CS913109 for *d14-1* (AT3G03990) mutant. All plants were grown in a growth chamber at 22 °C with a 16:8 h light/dark photoperiod. Sunshine Mix #1 Fafard 1P (Sungro Horticulture) was used to grow the plants. Following floral-dip transformation, transgenic plants were selected by germination on solid medium supplied with one-half Murashige & Skoog salt mixture without MES (Caisson Labs, catalogue no. MSP01) and kanamycin. Fifteen individual T1 plant lines were screened for phenotypes for each construct. Identification of CRISPR–Cas9-edited plants was performed by sequencing analyses of *MAX2-CTH* encoding region as similarly described in Swinnen et al.[72], with T2 lines screened for the absence of *cas9*. Analyses were conducted using representative homozygote T3 plant lines.

Hypocotyl length, leaf morphology, stem thickness and leaf senescence assays. Rosette leaves of equal size and developmental stage (leaf number 10–12) from 5-week-old plants, grown on soil, were collected and placed on a wet filter paper inside a Petri dish for a 7 d of dark incubation. Leaves were weighed and placed in 1 ml of *N*,*N*-dimethylformamide overnight. Chlorophyll was extracted and measured spectrophotometrically at 647 and 664 nm[74,75]. Chlorophyll concentration per gram of leaf tissue was calculated using the formula:

Chlorophyll concentration $(mg \times g^{-1}) = (20.27 \times A_{647}) + (7.04 \times A_{664}) \times g^{-1}$.

The hypocotyl length of 10-d-old seedlings, grown on plates under 24-h white light conditions, was measured using Fiji[76].

For leaf blade size, the seventh leaf of each plant was marked with indelible marker 3 weeks post germination. It was later measured at 35 and 37 d post germination to confirm leaf growth arrest. The length and maximum width of the blade were measured using Fiji[76].

The diameter of the basal internode of the primary inflorescence was measured at global proliferative arrest (8 weeks after germination) using a carbon fibre composite digital caliper.

Differential scanning fluorimetry. Samples were prepared in triplicate using 10 µM protein, incubated with 50 mM citrate (pH 6) in a buffer containing 20 mM HEPES, 150 mM Nacl and 1 mM tris(2-carboxyethyl)phosphine (TCEP). Following 20 min of incubation with the ligand, 0.5 mM Sypro Orange was added and used as the reporter dye. Following a 5-min equilibration at 4 °C, samples were heat denatured using a linear 4 to 95 °C gradient at a rate of 1 °C min^{-1}. Protein unfolding was monitored by detecting changes in Sypro Orange fluorescence using a Bio-Rad CFX96 real-time system with HEX emission (533 nm) and excitation (559 nm) fluorophore settings.

YLG hydrolysis assays. YLG (ThermoFisher Scientific) hydrolysis assays were conducted in 50 µl of reaction buffer (50 mM MES pH 6.0, 150 mM NaCl and 1 mM dithiothreitol) in a 96-well, F-bottom, black plate (Greiner), in accordance with the manufacturer's instructions. The intensity of the fluorescence was measured using a Synergy Microplate Reader (BioTek) with excitation at 480 nm and detection at 520 nm. Readings were collected at 14-s intervals over 60 min. Fluorescence data were converted directly to fluorescein concentration using a standard curve. In all experiments, 2 µM of D14 was added to a reaction containing 3 µM YLG, and 10 µM of ASK1–D3, ASK1–$D3^{D720K}$ or the equivalent buffer. In hydrolysis experiments containing organic acids, 50 µM of citrate or succinate (pH 6) were added to the reaction. GraphPad Prism v.9 was used to analyse the data. All experiments were repeated in triplicate.

Protein preparation and purification. Full-length rice D3 or the mutant in the CTH (*Oryza sativa*) and *A. thaliana* ASK1 were co-expressed as a 6×His–2×Msb (msyB) fusion protein and an untagged protein, respectively, in Hi5 suspension insect cells (as described ref. [22]). The ASK1–D3/$D3^{D720K}$ (D3 or D3 with D720K mutation) complex was isolated from the soluble cell lysate using Q Sepharose High Performance resin (GE Healthcare). The 600 mM NaCl eluates were further subjected to Ni Sepharose Fast Flow (GE Healthcare) and eluted with 200 mM imidazole. In experiments in which the 6×His–2×Msb fusion tag was removed, the clarified ASK1–D3/$D3^{D720K}$ complex was cleaved at 4 °C for 16 h using tobacco etch virus (TEV) protease, and purified by anion-exchange and size-exclusion chromatography. For crystallization and biochemical analysis, both D3-expressing constructs were designed to eliminate a non-conserved 40-residue disordered loop between amino acids 476 and 514 after affinity purification (as described in ref. [22]). The resulting D3 HisMsb fusion protein contains three TEV cleavage sites: between the Msb tag and D3, after T476, and before L514, resulting in a purified split stable form of D3 with D3–NTD (1–476) and CTD (514–720).

GST–$D53_{D2}$, GST–D14 and His-SUMO–D14 were expressed as fusion proteins in BL21 (DE3) cells. GST–$SMAXL7_{D2}$ and GST–$AUX/IAA17_{D2}$ were cloned and expressed as fusion proteins in BL21 (DE3) cells. Plasmid construction and protein purifications are detailed in Shabek et al.[22]. BL21 (DE3) cells transformed with the expression plasmid were grown in Luria Bertani broth at 16 °C to an OD_{600} of ~0.8 and induced with 0.25 mM isopropyl-β-D-thiogalactoside for 16 h. Cells were harvested, resuspended and lysed in extract buffer (20 or 50 mM Tris, pH 8.0, 200 mM NaCl). For GST-fused proteins, glutathione Sepharose (GE Healthcare) was used to isolate the proteins supplement with buffer containing 50 mM Tris–HCl, pH 8.0, 200 mM NaCl and 5 mM dithiothreitol. Proteins were purified by either elution with 5–8 mM glutathione (Fisher BioReagents), or on-column cleavage by TEV protease, followed by anion-exchange and size-exclusion chromatography. Rice D14 protein (*O. sativa*, residues 52–318) was expressed as a 6× His-SUMO fusion protein using the expression vector pSUMO (LifeSensors). His-SUMO–D14 was isolated from by Ni-NTA resin and the eluted His-SUMO–D14 was further separated by anion-exchange chromatography. In experiments in which the His-SUMO tag is removed, His-SUMO–D14 was further incubated overnight with SUMO protease (Ulp1, LifeSensors) at a protease to protein ratio of 1:1,000 at 4 °C, and the tag was removed by passing through Ni Sepharose. All proteins were further purified by chromatography by Superdex-200 gel filtration and concentrated by ultrafiltration to 3–10 mg ml^{-1}.

Trypsin-limited proteolytic digestion. Purified ASK1–D3 or ASK1–$D3^{D720K}$ (1 mg ml^{-1}) was incubated at 22 °C for 15 min with trypsin solution containing 1 µg ml^{-1} trypsin (Goldbio T-160) at 50 mM MES, pH 6.5, and 1 mM dithiothreitol. The proteolysis reactions were stopped by a fourfold concentration of SDS–PAGE sample buffer, followed immediately by 5 min boiling at 95 °C. Proteins were resolved by SDS–PAGE and Coomassie stain. The resolved bands corresponding to ASK1 and digested D3–CTD were excised and further analysed by N-terminal sequencing (UC Davis).

Pulldown assay. GST-tagged proteins were expressed in BL21 cells. Following cell lysis, clarification and centrifugation, the cell lysate was incubated with GST beads for 2 h at 4 °C. Beads were than washed twice with wash buffer containing 50 mM Tris, 150 mM NaCl, 1% glycerol and 1 mM TCEP. Beads were then washed once with 0.025% BSA blocking solution and twice with wash buffer. For the control, GST beads were incubated with 0.05% BSA. Protein-bound GST beads were incubated with purified His-tagged and or non-tagged proteins and 100 µM GR24 (or acetone as a control) for 30 min on ice. Following two washes with wash buffer, elution was achieved with 50 mM Tris, 10 mM reduced glutathione pH 7.2, and 5 mM dithiothreitol. After addition of fourfold concentrated sample buffer, boiled samples were resolved via SDS–PAGE, and proteins were visualized using Ponceau stain as well as western blotting with monoclonal anti-His (Invitrogen, catalogue no. MA1-21315) and polyclonal anti-GST (ThermoFisher Scientific, catalogue no. CAB4169) antibodies.

Plant cell-free degradation and ubiquitination. A 150-mg sample of inflorescences of *Arabidopsis* ecotype Columbia-0 (Col-0) WT and *max2-2* mutant and *pUB:*$MAX2^{D693K}$ plants were collected and frozen. Total proteins were extracted to a stock concentration of 8–10 mg ml^{-1} using Mintue (Invent Biotechnologies, catalogue no. SD-008/SN-009), supplemented with protease inhibitor cocktail (Roche). To monitor protein degradation in the cell-free system, 0.5 µg of purified tagged proteins were incubated at 22 °C in a reaction mixture that contained, in a final volume of 12.5 µl, 3 µl of plant extract supplemented with 10 µM GR24, 25 mM Tris–HCl, pH 7.4, 0.625 mM ATP, 5 mM $MgCl_2$, 0.25 µg $µl^{-1}$ Ub and 0.5 mM dithiothreitol. To test the effect of organic acids, samples were incubated with 50 mM of citrate or succinate. Where indicated, the proteasome inhibitor MG132 (ThermoFisher Scientific, catalogue no. 47-479-01MG) was used as described previously[22]. Reactions were terminated at the indicated times by the addition of fourfold concentrated sample buffer. Boiled samples were resolved via SDS–PAGE, and proteins were visualized using western blotting and polyclonal anti-GST antibodies.

For the cell-free ubiquitination assay, a similar protocol was performed using GST-tagged protein with the addition of 1 µM MG132 to all samples to inhibit degradation. *max2* plant protein extract was supplemented with 0.5 µg of purified His-D3 or His-$D3^{D720K}$ (both were co-purified with ASK1). WT plant protein extract was incubated with 50 mM citrate or succinate. Following 1 h of incubation in 27 °C, pulldown using GST beads was completed. Beads were washed twice with 50 mM Tris, 150 mM NaCl, 1% glycerol and 1 mM TCEP. Elution was achieved with 50 mM Tris, 10 mM reduced glutathione, pH 7.2, and 5 mM dithiothreitol. After addition of fourfold concentrated sample buffer, boiled samples were resolved via SDS–PAGE, and proteins were visualized using western blotting and monoclonal anti-ubiquitin antibody (ThermoFisher Scientific, catalogue no. eBioP4D1 (p4D1)). High molecular mass conjugated Ub species were quantified and normalized by their intensity compared with the non-conjugated GST–$D53_{D2}$ species. Quantification of bands was performed using Image Lab v.6.0.1 (Bio-Rad).

Crystallization, data collection and structure determination. Crystals of ASK1–$D3^{D720K}$ were grown at 22 °C by the hanging-drop vapour diffusion method with 2.0 µl of protein sample mixed with 1.0 µl of a reservoir solution containing 0.1 M ammonium acetate, 0.1 M sodium formate, 0.1 M sodium citrate tribasic dihydrate, 0.1 M potassium sodium tartrate tetrahydrate, 0.1 M sodium oxamate, 0.1 M Tris, 0.1 M bicine and 30% PEG 500 MME and PEG20000 at pH 8.5. Crystals of maximal sizes were obtained and collected after 2 weeks. X-ray diffraction data were integrated and scaled using the HKL2000 package[77]. The crystals were determined by molecular replacement with the ASK1–D3-engaged state (6BRP) as the search model using PHENIX[78]. All structural models were manually built, refined and rebuilt with PHENIX and COOT.

Ligand fit using AutoDock Vina. The receptor and ligand file containing the atomic charges, atom types and topology information are prepared using the scripts from AutoDock-MGL tools[79,80]. The ligand interaction map was calculated with the help of the program autogrid before docking of the ligand to the receptor. The size and the exact position of the autogrid box was adjusted to the centre of the amino acid residue R40 and R36 of receptor. The different ligands were allowed to dock within the defined site on the receptor using AutoDock Vina. The top ranked ligand pose for each ligand were chosen and analysed using PyMOL.

Molecular dynamics simulation. The molecular dynamics simulation was performed using GROMACS v.2020 (ref. [81]). Using standard settings adapted from Martini v.2.2 (ref. [31]). Missing residues and atoms of the crystallized ASK1–D3 and ASK1–$D3^{D720K}$ complex were built using the homology modelling tool, swissmodeller[82]. The simulation was initiated by solvating each protein complex in a cubic simulation box with 1.2 nm between the box edge and the protein. The amounts of total charge for ASK1–D3 and ASK1–$D3^{D720K}$ were analysed and counterions were added to each system to neutralize the charge of the protein followed by short-energy minimization using the steepest descent method for 1000 ps. Pre-equilibration was preformed using the inbuilt relaxation protocol. The whole system was subjected to 1 ms simulation. Calculation of the r.m.s.d., r.m.s.f. and cluster analysis were carried out to analyse changes in the structure and dynamics of the CTH of the ASK1–D3 and ASK1–$D3^{D720K}$ complexes.

Statistical analysis and reproducibility. All analyses were performed using GraphPad Prism v.9. Statistical tests, samples sizes, *P* values and degrees of significance (***$P < 0.001$; **$P < 0.01$; *$P < 0.05$) are described in the figure legends.

Departure from normal distribution was tested using combined data from experimental replicates with the Shapiro–Wilk test ($P > 0.05$). One-way analysis of variance (ANOVA) tests were conducted following by Tukey–Kramer honestly significant difference post hoc tests. Before Student's *t* tests, data were tested for

equal variance by *F*-tests. No statistical methods were used to predetermine sample size. All pulldown and in vitro degradation assays were repeated independently three times with similar results.

Reporting Summary. Further information on research design is available in the Nature Research Reporting Summary linked to this article.

Data availability

The atomic coordinates and all related data of ASK1–D3 mutant structure were deposited in the Protein Data Bank with accession code 7SA1 (PDB:7SA1). All other materials are available from the corresponding author upon request. Source data are provided with this paper.

Received: 22 September 2021; Accepted: 28 March 2022;
Published online: 28 April 2022

References

1. Stirnberg, P., van De Sande, K. & Leyser, H. M. O. MAX1 and MAX2 control shoot lateral branching in *Arabidopsis*. *Development* **129**, 1131–1141 (2002).
2. Stirnberg, P., Furner, I. J. & Ottoline Leyser, H. M. MAX2 participates in an SCF complex which acts locally at the node to suppress shoot branching. *Plant J.* **50**, 80–94 (2007).
3. Umehara, M. et al. Inhibition of shoot branching by new terpenoid plant hormones. *Nature* **455**, 195–200 (2008).
4. Gomez-Roldan, V. et al. Strigolactone inhibition of shoot branching. *Nature* **455**, 189–194 (2008).
5. Cook, C. E., Whichard, L. P., Turner, B., Wall, M. E. & Egley, G. H. Germination of witchweed (*Striga lutea* Lour.): isolation and properties of a potent stimulant. *Science* **154**, 1189–1190 (1966).
6. Akiyama, K., Matsuzaki, K. & Hayashi, H. Plant sesquiterpenes induce hyphal branching in arbuscular mycorrhizal fungi. *Nature* **435**, 824–827 (2005).
7. Shabek, N. & Zheng, N. Plant ubiquitin ligases as signaling hubs. *Nat. Struct. Mol. Biol.* **21**, 293–296 (2014).
8. Arite, T. et al. d14, a strigolactone-insensitive mutant of rice, shows an accelerated outgrowth of tillers. *Plant Cell Physiol.* **50**, 1416–1424 (2009).
9. Hamiaux, C. et al. DAD2 is an α/β hydrolase likely to be involved in the perception of the plant branching hormone, strigolactone. *Curr. Biol.* **22**, 2032–2036 (2012).
10. Ishikawa, S. et al. Suppression of tiller bud activity in tillering dwarf mutants of rice. *Plant Cell Physiol.* **46**, 79–86 (2005).
11. Jiang, L. et al. DWARF 53 acts as a repressor of strigolactone signalling in rice. *Nature* **504**, 401–405 (2013).
12. Zhou, F. et al. D14-SCF D3-dependent degradation of D53 regulates strigolactone signalling. *Nature* **504**, 406–410 (2013).
13. Soundappan, I. et al. SMAX1-LIKE/D53 family members enable distinct MAX2-dependent responses to strigolactones and karrikins in *Arabidopsis*. *Plant Cell* **27**, 3143–3159 (2015).
14. Wang, L. et al. Strigolactone signaling in *Arabidopsis* regulates shoot development by targeting D53-like SMXL repressor proteins for ubiquitination and degradation. *Plant Cell* **27**, 3128–3142 (2015).
15. Liang, Y., Ward, S., Li, P., Bennett, T. & Leyser, O. SMAX1-LIKE7 signals from the nucleus to regulate shoot development in *Arabidopsis* via partially EAR motif-independent mechanisms. *Plant Cell* **28**, 1581–1601 (2016).
16. Wang, L. et al. Transcriptional regulation of strigolactone signalling in *Arabidopsis*. *Nature* **583**, 277–281 (2020).
17. Tal, L., Anleu Gil, M. X., Guercio, A. M. & Shabek, N. Structural aspects of plant hormone signal perception and regulation by ubiquitin ligases. *Plant Physiol.* **182**, 1537–1544 (2020).
18. Tan, X. et al. Mechanism of auxin perception by the TIR1 ubiquitin ligase. *Nature* **446**, 640–645 (2007).
19. Sheard, L. B. et al. Jasmonate perception by inositol-phosphate-potentiated COI1-JAZ co-receptor. *Nature* **468**, 400–405 (2010).
20. Carlsson, G. H., Hasse, D., Cardinale, F., Prandi, C. & Andersson, I. The elusive ligand complexes of the DWARF14 strigolactone receptor. *J. Exp. Bot.* **69**, 2345–2354 (2018).
21. Yao, R. et al. DWARF14 is a non-canonical hormone receptor for strigolactone. *Nature* **536**, 469–473 (2016).
22. Shabek, N. et al. Structural plasticity of D3–D14 ubiquitin ligase in strigolactone signalling. *Nature* **563**, 652–656 (2018).
23. de Saint Germain, A. et al. An histidine covalent receptor and butenolide complex mediates strigolactone perception. *Nat. Chem. Biol.* **12**, 787–794 (2016).
24. Seto, Y. et al. Strigolactone perception and deactivation by a hydrolase receptor DWARF14. *Nat. Commun.* **10**, 191 (2019).
25. Stanga, J. P., Smith, S. M., Briggs, W. R. & Nelson, D. C. SUPPRESSOR OF MORE AXILLARY GROWTH2 1 controls seed germination and seedling development in *Arabidopsis*. *Plant Physiol.* **163**, 318–330 (2013).
26. Waters, M. T. et al. Specialisation within the DWARF14 protein family confers distinct responses to karrikins and strigolactones in *Arabidopsis*. *Development* **139**, 1285–1295 (2012).
27. Swarbreck, S. M., Guerringue, Y., Matthus, E., Jamieson, F. J. C. & Davies, J. M. Impairment in karrikin but not strigolactone sensing enhances root skewing in *Arabidopsis thaliana*. *Plant J.* **98**, 607–621 (2019).
28. Stanga, J. P., Morffy, N. & Nelson, D. C. Functional redundancy in the control of seedling growth by the karrikin signaling pathway. *Planta* **243**, 1397–1406 (2016).
29. Wang, L. et al. Strigolactone and karrikin signaling pathways elicit ubiquitination and proteolysis of SMXL2 to regulate hypocotyl elongation in *Arabidopsis*. *Plant Cell* **32**, 2251–2270 (2020).
30. Marrink, S. J., Risselada, H. J., Yefimov, S., Tieleman, D. P. & de Vries, A. H. The MARTINI force field: coarse grained model for biomolecular simulations. *J. Phys. Chem. B* **111**, 7812–7824 (2007).
31. Uusitalo, J. J., Ingólfsson, H. I., Akhshi, P., Tieleman, D. P. & Marrink, S. J. Martini coarse-grained force field: extension to DNA. *J. Chem. Theory Comput.* **11**, 3932–3945 (2015).
32. Ueda, H. & Kusaba, M. Strigolactone regulates leaf senescence in concert with ethylene in *Arabidopsis*. *Plant Physiol.* **169**, 138–147 (2015).
33. Bennett, T. et al. Strigolactone regulates shoot development through a core signalling pathway. *Biol. Open* **5**, 1806–1820 (2016).
34. Jia, K. P., Luo, Q., He, S. B., Lu, X. D. & Yang, H. Q. Strigolactone-regulated hypocotyl elongation is dependent on cryptochrome and phytochrome signaling pathways in *Arabidopsis*. *Mol. Plant* **7**, 528–540 (2014).
35. Song, C. et al. Strigo-D2—a bio-sensor for monitoring the spatio-temporal pattern of strigolactone signaling in intact plants. *Plant Physiol.* **188**, 97–110 (2022).
36. Wang, Y. et al. Molecular basis for high ligand sensitivity and selectivity of strigolactone receptors in *Striga*. *Plant Physiol.* **185**, 1411–1428 (2021).
37. Zhou, F. et al. D14-SCF D3-dependent degradation of D53 regulates strigolactone signalling. *Nature* **504**, 406–410 (2013).
38. Khosla, A. et al. Structure–function analysis of SMAX1 reveals domains that mediate its karrikin-induced proteolysis and interaction with the receptor KAI2. *Plant Cell* **32**, 2639–2659 (2020).
39. Chevalier, F. et al. Strigolactone promotes degradation of DWARF14, an α/β hydrolase essential for strigolactone signaling in *Arabidopsis*. *Plant Cell* **26**, 1134–1150 (2014).
40. Hu, Q. et al. DWARF14, a receptor covalently linked with the active form of strigolactones, undergoes strigolactone-dependent degradation in rice. *Front. Plant Sci.* **8**, 1935 (2017).
41. Hu, X. et al. Expanding the range of CRISPR/Cas9 genome editing in rice. *Mol. Plant* **9**, 943–945 (2016).
42. Alessandri, R. et al. Pitfalls of the Martini model. *J. Chem. Theory Comput.* **15**, 5448–5460 (2019).
43. Qian, S. B. et al. Engineering a ubiquitin ligase reveals conformational flexibility required for ubiquitin transfer. *J. Biol. Chem.* **284**, 26797–26802 (2009).
44. Baek, K. et al. NEDD8 nucleates a multivalent cullin–RING–UBE2D ubiquitin ligation assembly. *Nature* **578**, 461–466 (2020).
45. Wu, S. et al. CAND1 controls in vivo dynamics of the cullin 1-RING ubiquitin ligase repertoire. *Nat. Commun.* **4**, 1642 (2013).
46. Rusnac, D.-V. & Zheng, N. in *Cullin-RING Ligases and Protein Neddylation: Biology and Therapeutics* (eds. Sun, Y. et al.) 9–31 (Springer, 2020).
47. Verdecia, M. A. et al. Conformational flexibility underlies ubiquitin ligation mediated by the WWP1 HECT domain E3 ligase. *Mol. Cell* **11**, 249–259 (2003).
48. Russell, R. J. M., Ferguson, J. M. C., Hough, D. W., Danson, M. J. & Taylor, G. L. The crystal structure of citrate synthase from the hyperthermophilic archaeon *Pyrococcus furiosus* at 1.9 Å resolution. *Biochemistry* **36**, 9983–9994 (1997).
49. Hicks, K. G. et al. Protein–metabolite interactomics reveals novel regulation of carbohydrate metabolism. Preprint at *bioRxiv* https://doi.org/10.1101/2021.08.28.458030 (2021).
50. Diether, M. & Sauer, U. Towards detecting regulatory protein–metabolite interactions. *Curr. Opin. Microbiol.* **39**, 16–23 (2017).
51. Bennett, B. D. et al. Absolute metabolite concentrations and implied enzyme active site occupancy in *Escherichia coli*. *Nat. Chem. Biol.* **5**, 593–599 (2009).
52. Ahn, E., Kumar, P., Mukha, D., Tzur, A. & Shlomi, T. Temporal fluxomics reveals oscillations in TCA cycle flux throughout the mammalian cell cycle. *Mol. Syst. Biol.* **13**, 953 (2017).
53. Wittmann, C., Hans, M., van Winden, W. A., Ras, C. & Heijnen, J. J. Dynamics of intracellular metabolites of glycolysis and TCA cycle during cell-cycle-related oscillation in *Saccharomyces cerevisiae*. *Biotechnol. Bioeng.* **89**, 839–847 (2005).
54. Lee, C. P. et al. The versatility of plant organic acid metabolism in leaves is underpinned by mitochondrial malate–citrate exchange. *Plant Cell* **33**, 3700–3720 (2021).
55. Martínez-Reyes, I. & Chandel, N. S. Mitochondrial TCA cycle metabolites control physiology and disease. *Nat. Commun.* **11**, 102 (2020).

56. Quandt, E. M. et al. Fine-tuning citrate synthase flux potentiates and refines metabolic innovation in the Lenski evolution experiment. *eLife* **4**, e09696 (2015).
57. Fürtauer, L., Küstner, L., Weckwerth, W., Heyer, A. G. & Nägele, T. Resolving subcellular plant metabolism. *Plant J.* **100**, 438–455 (2019).
58. Sulpice, R. & McKeown, P. C. Moving toward a comprehensive map of central plant metabolism. *Annu. Rev. Plant Biol.* **66**, 187–210 (2015).
59. López-Bucio, J., de la Vega, O. M., Guevara-García, A. & Herrera-Estrella, L. Enhanced phosphorus uptake in transgenic tobacco plants that overproduce citrate. *Nat. Biotechnol.* **18**, 450–453 (2000).
60. Brewer, P. B., Koltai, H. & Beveridge, C. A. Diverse roles of strigolactones in plant development. *Mol. Plant* **6**, 18–28 (2013).
61. Liu, G. et al. Changes in the allocation of endogenous strigolactone improve plant biomass production on phosphate-poor soils. *New Phytol.* **217**, 784–798 (2018).
62. Saeed, W., Naseem, S. & Ali, Z. Strigolactones biosynthesis and their role in abiotic stress resilience in plants: a critical review. *Front. Plant Sci.* **8**, 1487 (2017).
63. Tahjib-Ul-Arif, M. et al. Citric acid-mediated abiotic stress tolerance in plants. *Int. J. Mol. Sci.* **22**, 7235 (2021).
64. Besserer, A. et al. Strigolactones stimulate arbuscular mycorrhizal fungi by activating mitochondria. *PLoS Biol.* **4**, e226 (2006).
65. Kihara, T., Wada, T., Suzuki, Y., Hara, T. & Koyama, H. Alteration of citrate metabolism in cluster roots of white lupin. *Plant Cell Physiol.* **44**, 901–908 (2003).
66. Proost, S. et al. PLAZA 3.0: an access point for plant comparative genomics. *Nucleic Acids Res.* **43**, D974–D981 (2015).
67. Bailey, T. L. et al. MEME Suite: tools for motif discovery and searching. *Nucleic Acids Res.* **37**, W202–W208 (2009).
68. Geldner, N. et al. Rapid, combinatorial analysis of membrane compartments in intact plants with a multicolor marker set. *Plant J.* **59**, 169–178 (2009).
69. Unger, T., Jacobovitch, Y., Dantes, A., Bernheim, R. & Peleg, Y. Applications of the Restriction Free (RF) cloning procedure for molecular manipulations and protein expression. *J. Struct. Biol.* **172**, 34–44 (2010).
70. Gleave, A. P. A versatile binary vector system with a T-DNA organisational structure conducive to efficient integration of cloned DNA into the plant genome. *Plant Mol. Biol.* **20**, 1203–1207 (1992).
71. Fauser, F., Schiml, S. & Puchta, H. Both CRISPR/Cas-based nucleases and nickases can be used efficiently for genome engineering in *Arabidopsis thaliana*. *Plant J.* **79**, 348–359 (2014).
72. Swinnen, G., Jacobs, T., Pauwels, L. & Goossens, A. in *Plant and Food Carotenoids: Methods and Protocols* (eds. Rodríguez-Concepción, M. & Welsch, R.) 321–341 (Humana, 2020).
73. Swinnen, G. et al. Constitutive steroidal glycoalkaloid biosynthesis in tomato is regulated by the clade IIIe basic helix–loop–helix transcription factors MYC1 and MYC2. Preprint at *bioRxiv* https://doi.org/10.1101/2020.01.27.921833 (2020).
74. Porra, R. J., Thompson, W. A. & Kriedemann, P. E. Determination of accurate extinction coefficients and simultaneous equations for assaying chlorophylls a and b extracted with four different solvents: verification of the concentration of chlorophyll standards by atomic absorption spectroscopy. *Biochim. Biophys. Acta Bioenerg.* **975**, 384–394 (1989).
75. Inskeep, W. P. & Bloom, P. R. Extinction coefficients of chlorophyll a and b in *N*,*N*-dimethylformamide and 80% acetone 1. *Plant Physiol.* **77**, 483–485 (1985).
76. Schneider, C. A., Rasband, W. S. & Eliceiri, K. W. NIH Image to ImageJ: 25 years of image analysis. *Nat. Methods* **9**, 671–675 (2012).
77. Otwinowski, Z. & Minor, W. B. T.-M. in *Methods in Enzymology* Vol. 276, 307–326 (Academic Press, 1997).
78. Adams, P. D. et al. PHENIX: a comprehensive Python-based system for macromolecular structure solution. *Acta Crystallogr. D* **66**, 213–221 (2010).
79. Sanner, M. Python: a programming language for software integration and development. *J. Mol. Graph. Model.* **17** **1**, 57–61 (1999).
80. Trott, O. & Olson, A. J. AutoDock Vina: improving the speed and accuracy of docking with a new scoring function, efficient optimization, and multithreading. *J. Comput. Chem.* **31**, 455–461 (2010).
81. Kutzner, C. et al. More bang for your buck: Improved use of GPU nodes for GROMACS 2018. *J. Comput. Chem.* **40**, 2418–2431 (2019).
82. Bordoli, L. et al. Protein structure homology modeling using SWISS-MODEL workspace. *Nat. Protoc.* **4**, 1–13 (2009).

Acknowledgements

N.S. is supported by National Science Foundation, NSF-CAREER (Award No. 2047396) and NSF-EAGER (Award No. 2028283). We thank the beamline staff for providing technical assistance at the Advanced Light Source (U.S. Department of Energy Office of Science User Facility under Contract No. DE-AC02-05CH11231, supported in part by the ALS-ENABLE program funded by the National Institutes of Health, National Institute of General Medical Sciences, grant P30 GM124169-01). A.B.'s laboratory is supported by National Science Foundation, NSF BTT EAGER (Award No. 1844705). L.T. is supported by BARD, the United States–Israel Binational Agricultural Research and Development Fund, Vaadia-BARD Postdoctoral Fellowship Award FI-559-2017.

Author contributions

L.T. and N.S. conceived and designed the experiments. N.S. and L.T. conducted the protein purification, biochemical and crystallization experiments with the help of A.Y. and M.P. Structural and functional analyses were determined and performed by N.S., L.T. and M.P. N.S. and M.P. designed and performed molecular dynamics simulations. N.S. and L.T. designed, and L.T. generated the transgenic lines including phenotype characterizations. L.T., M.R. and A.B. designed and L.T. generated CRISPR–Cas9 *Arabidopsis* lines. N.S. and L.T. wrote the manuscript with the help from M.P., M.R. and A.B.

Competing interests

N.S. has an equity interest in Oerth Bio and serves on the company's Scientific Advisory Board. The work and data submitted here have no competing interests, nor other interests that might be perceived to influence the results and/or discussion reported in this paper. The remaining authors declare no competing interests.

Additional information

Extended data is available for this paper at https://doi.org/10.1038/s41477-022-01145-7.

Supplementary information The online version contains supplementary material available at https://doi.org/10.1038/s41477-022-01145-7.

Correspondence and requests for materials should be addressed to Nitzan Shabek.

Peer review information *Nature Plants* thanks Tom Bennett, Shinjiro Yamaguchi and the other, anonymous, reviewers for their contribution to the peer review of this work.

Reprints and permissions information is available at www.nature.com/reprints.

Publisher's note Springer Nature remains neutral with regard to jurisdictional claims in published maps and institutional affiliations.

© The Author(s), under exclusive licence to Springer Nature Limited 2022

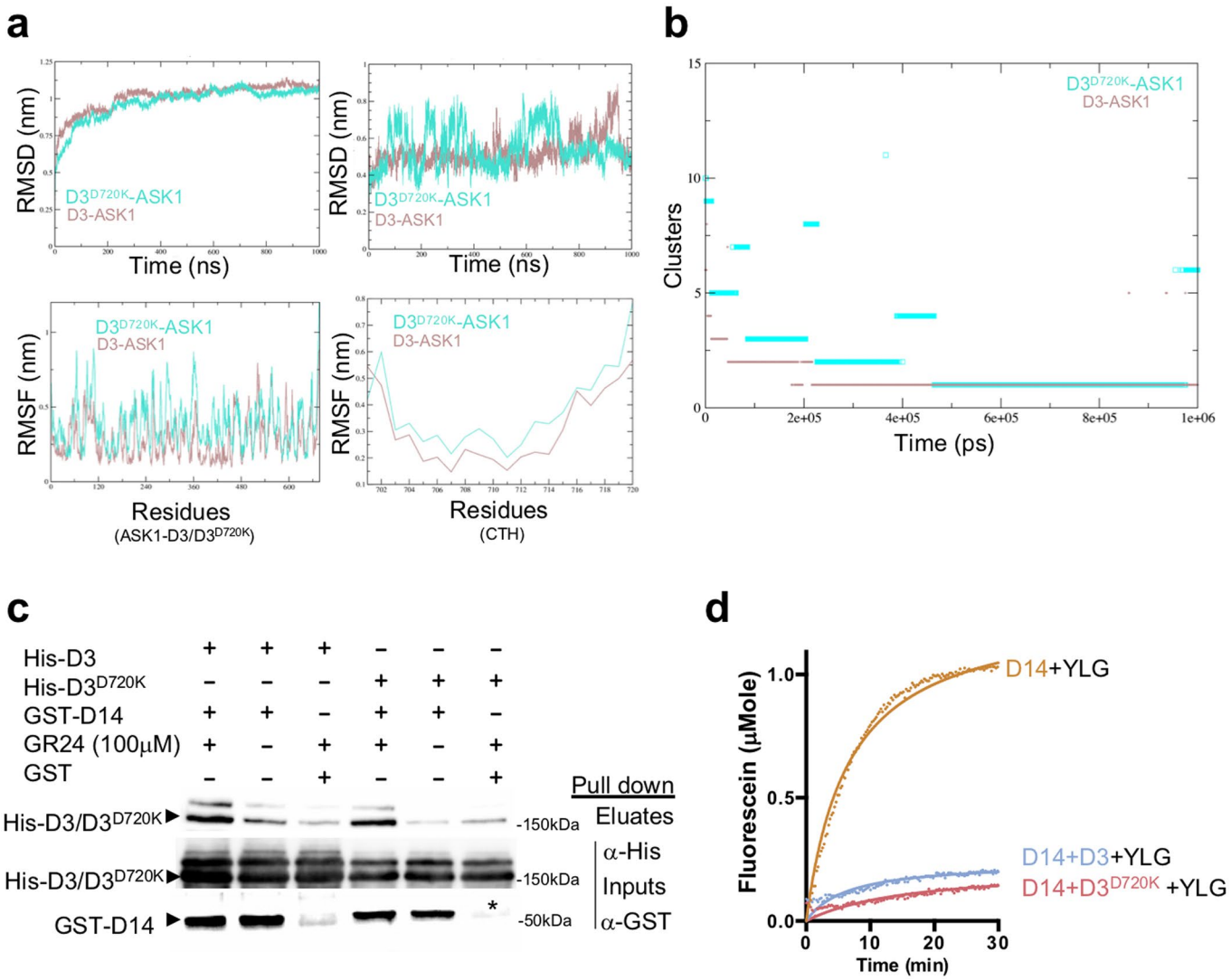

Extended Data Fig. 1 | Molecular dynamics simulation of ASK1-D3^{D720K} and functionality analyses. a, Molecular dynamics simulation of ASK1-D3 and ASK1-D3^{D720K}. Root mean square deviation (RMSD, upper panels) and RMS fluctuation (RMSF, lower panels) of all atoms plotted as a function of time for ASK-D3 (brown) and ASK1-D3^{D720K} (cyan) (left panels) and for the CTH of ASK-D3 and ASK1-D3^{D720K} (right panels). **b**, Conformational clusters over time plotted with the cut-off of 0.25 nm. **c**, Pulldown of GST-D14 and His-D3 or His-D3^{D720K} in the presence or absence of the synthetic SL, GR24. Proteins were resolved by SDS-PAGE and visualized via Western blot with anti-His and anti-GST antibodies. Asterisk denotes non-specific protein band. **d**, D14-YLG hydrolysis assay in the presence of either ASK1-D3, or ASK1-D3^{D720K}. Colored lines represent non-linear regression curved fit based on duplications of the raw data points (shown in dots).

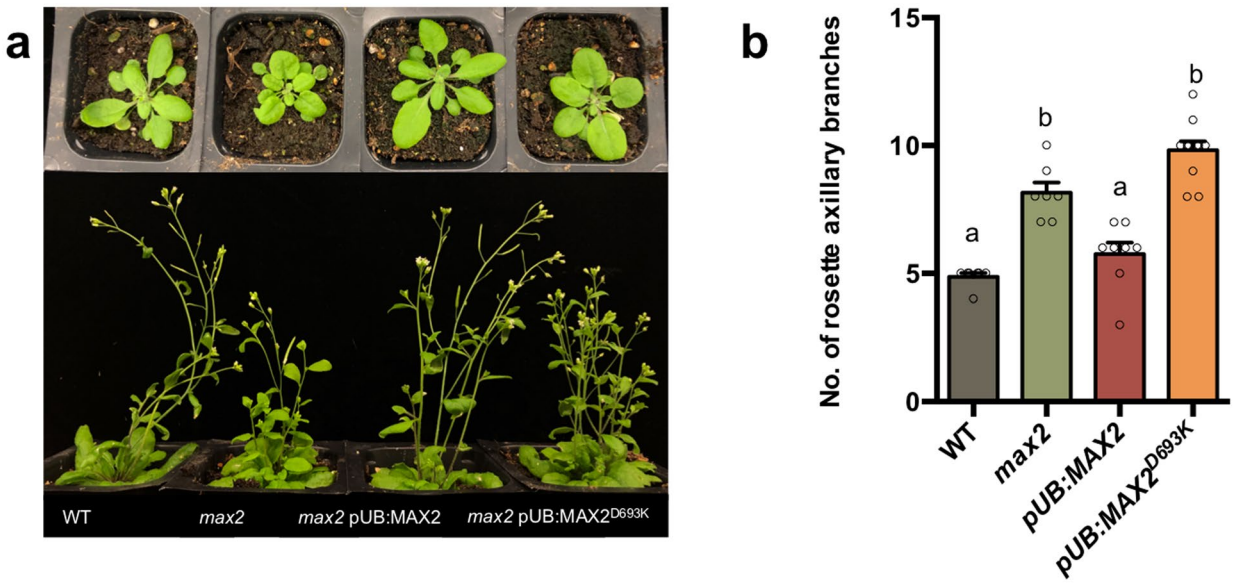

Extended Data Fig. 2 | *max2* complementation experiments. a, Top panel shows 5 week old plants, SL deficiency phenotypes include changes in rosettes size and leaf shape. Bottom panel shows 8 week old plants, an SL deficiency phenotype of excessive branching is shown. Transgenic plants are in *max2* background. **b**, Mean number of axillary rosettes branches (± SE). (WT (n = 7), *max2* (n = 7), *pUBQ:MAX2* (n = 8) and *pUBQ:MAX2*^{D693K} (n = 11), One-way ANOVA and post hoc Tukey test, $P < 0.001$). Transgenic plants are in *max2* background.

Extended Data Fig. 3 | D-pocket perturbed MAX2 plants. 5-week-old plants show SL deficiency phenotypes including changes in rosettes size and leaf shape (upper panel). 8-week-old plants exhibit SL deficiency phenotype of excessive branching (lower panel). Transgenic plants are in WT Col-0 background.

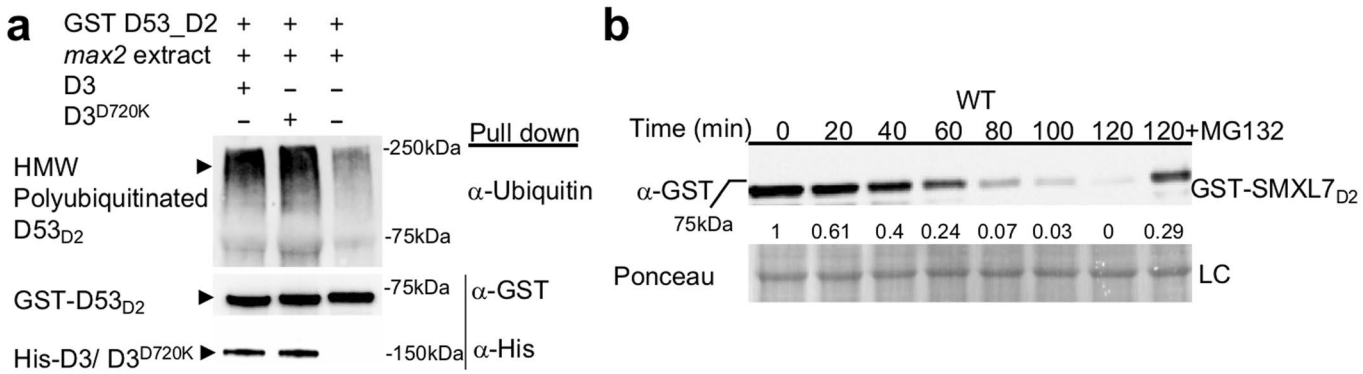

Extended Data Fig. 4 | Ubiquitination and time scale degradation of GST-SMXL7D2. a, Representative Western blot gel of a polyubiquitinated $D53_{D2}$ levels measurement using anti-GST (α-GST), anti-Ubiquitin (α-Ubiquitin) and anti-His (a-His) antibodies in the presence of *max2* total protein extract and His-D3 or His-$D3^{D720K}$. **b**, Time scale of cell-free degradation of GST-$SMXL7_{D2}$ in comparison to a sample incubated with protease inhibitor MG132. Loading control (LD) is shown by Ponceau stain.

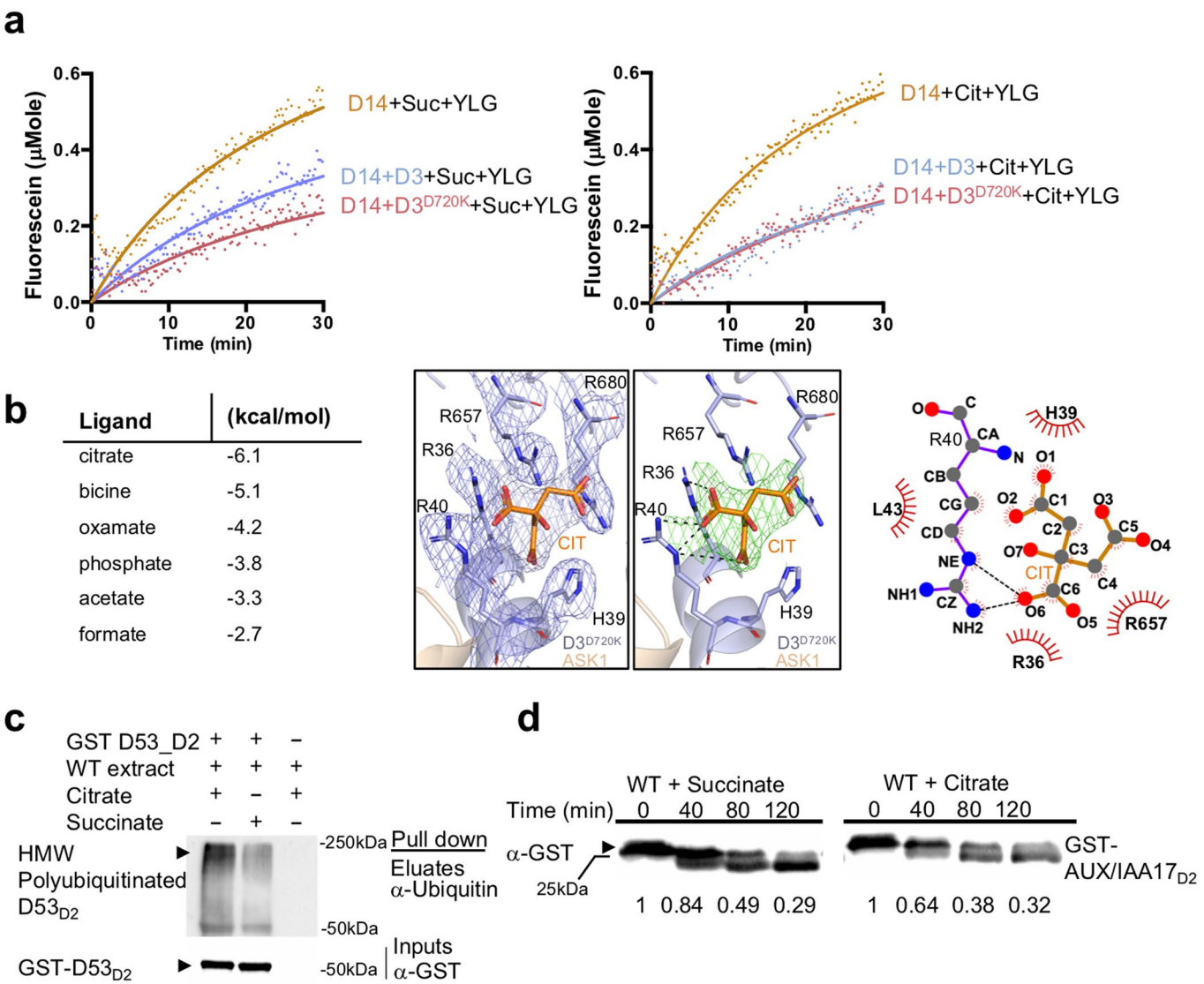

Extended Data Fig. 5 | functional analysis of ASK1-D3-citrate complex dynamics. a, D14-YLG hydrolysis assay in the presence of either ASK1-D3, or ASK1-D3^{D720K}, and succinate (Suc, left) or citrate (Cit, right) as indicated. Colored lines represent non-linear regression curved fit based on duplications of the raw data points (shown in dots). **b**, Molecular docking, and fitting scores of the different ligands from ASK1-D3^{D720K} crystallization conditions are shown in the table with DG values. Closeup view of the $2F_o$-F_c (1.0 s, left panel) map and F_o-F_c (3 s, right panel) show fitting of citrate into F_o-F_c electron density and its interaction with residues in the D-Pocket. 2-D interaction plot was generated using LigPlot+ and shows citrate interaction network with the D-pocket (black dash lines represent hydrogen bonds, arches represent Van der Waals interactions). **c**, Representative Western blot gel of a polyubiquitinated $D53_{D2}$ levels measurement using anti-GST (α-GST), anti-Ubiquitin (α -Ubiquitin) and anti-His (α -His) antibodies, in the presence of WT total protein extract with citrate or succinate **d**, Cell-free degradation of GST-AUX/IAA17$_{D2}$ detected by Western blot using anti-GST (α -GST) antibody. Numbers under the blots are proportions of protein remained that were quantified and compared to T = 0. The experiment was repeated three times.

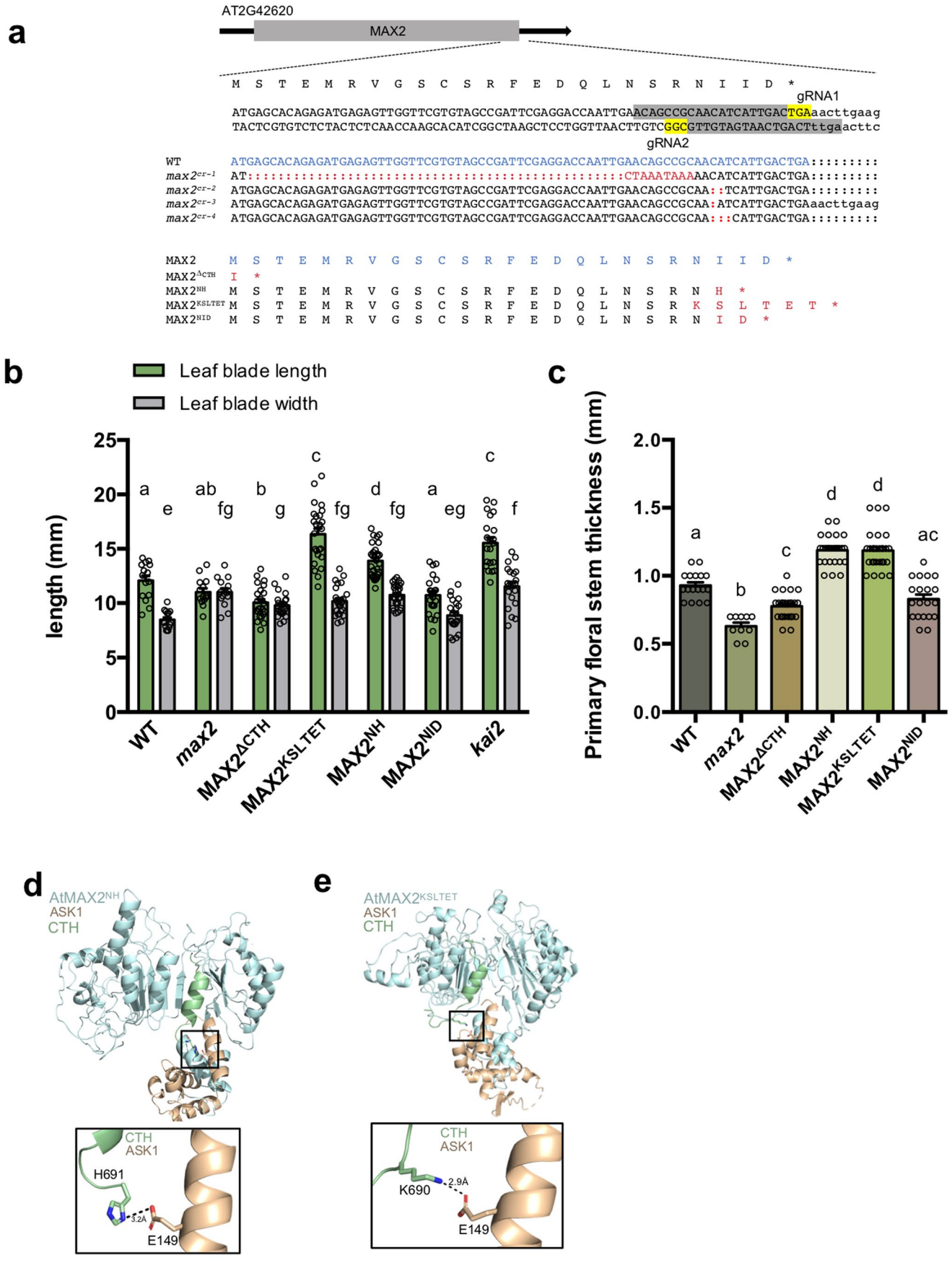

Extended Data Fig. 6 | See next page for caption.

Extended Data Fig. 6 | Genome edited MAX2 Arabidopsis lines. a, Schematic representation of MAX2 protein variants generated by CRISPR/Cas9. *MAX2* gene diagram is shown with focus on *MAX2* coding sequence for the CTH amino acids. gRNAs are colored in grey with PAM sequence colored yellow. All WT sequences are shown in blue. DNA deletions as well as protein sequence changes are shown in red. **b**, Mean leaf blade length and width in the 7th leaf of WT, *max2*, CRISPR/CAS9 edited MAX2 mutants and *kai2*. measured at proliferative arrest (± SE). WT (n = 15), *max2* (n = 14), MAX2$^{\Delta CTH}$ (n = 23), MAX2^{NH} (n = 25), MAX2^{KSLTET} (n = 29), MAX2^{NID} (n = 23) and *kai2* (n = 21); bars with the same letter are not significantly different from one another (One-way ANOVA and post hoc Tukey, $P < 0.05$). **c**, Mean of primary floral stem thickness of WT, *max2* and MAX2 genome edited CRISPR/CAS9 lines. (± SE). *n* = WT (n = 17), *max2* (n = 10), MAX2$^{\Delta CTH}$ (n = 28), MAX2^{NH} (n = 27), MAX2^{KSLTET} (n = 28) and MAX2^{NID} (n = 20); bars with the same letter are not significantly different from one another (One-way ANOVA and post hoc Tukey, $P < 0.05$). **d-e**, Structural simulations of AtMAX2 mutants reveal salt bridges between H691 ***(b)*** or K690 ***(c)*** of CTH and E149 of ASK1.

nature portfolio

Corresponding author(s): Nitzan Shabek

Last updated by author(s): Mar 23, 2022

Reporting Summary

Nature Portfolio wishes to improve the reproducibility of the work that we publish. This form provides structure for consistency and transparency in reporting. For further information on Nature Portfolio policies, see our Editorial Policies and the Editorial Policy Checklist.

Statistics

For all statistical analyses, confirm that the following items are present in the figure legend, table legend, main text, or Methods section.

n/a	Confirmed
☐	☒ The exact sample size (*n*) for each experimental group/condition, given as a discrete number and unit of measurement
☐	☒ A statement on whether measurements were taken from distinct samples or whether the same sample was measured repeatedly
☐	☒ The statistical test(s) used AND whether they are one- or two-sided *Only common tests should be described solely by name; describe more complex techniques in the Methods section.*
☒	☐ A description of all covariates tested
☐	☒ A description of any assumptions or corrections, such as tests of normality and adjustment for multiple comparisons
☐	☒ A full description of the statistical parameters including central tendency (e.g. means) or other basic estimates (e.g. regression coefficient) AND variation (e.g. standard deviation) or associated estimates of uncertainty (e.g. confidence intervals)
☐	☒ For null hypothesis testing, the test statistic (e.g. *F*, *t*, *r*) with confidence intervals, effect sizes, degrees of freedom and *P* value noted *Give P values as exact values whenever suitable.*
☒	☐ For Bayesian analysis, information on the choice of priors and Markov chain Monte Carlo settings
☒	☐ For hierarchical and complex designs, identification of the appropriate level for tests and full reporting of outcomes
☒	☐ Estimates of effect sizes (e.g. Cohen's *d*, Pearson's *r*), indicating how they were calculated

Our web collection on statistics for biologists contains articles on many of the points above.

Software and code

Policy information about availability of computer code

Data collection	Single crystal X-ray diffraction data were collected at Advanced Light Source (ALS) in Berkeley. The obtained data were integrated and scaled with HKL2000 (HKL2000_v721-Linux). The structure model was manually built, refined, and rebuilt with PHENIX (Phenix 1.18.2-3874) and COOT (COOT 0.9.7). Groma
Data analysis	Structure analysis were carried out using COOT (COOT 0.9.7), PyMOL (PyMOL (TM) 2.2.3), PHENIX (Phenix 1.18.2-3874). Biochemical analysis were performed with GraphPad Prism 9 Software. Hypocotyl length was measured using Fiji (1.53c) . Protein bands were quantified using Image lab 6.0.1. MD simulations and analyses were preformed using Gromacs (v2020.3) and the graph plotted with Grace (v5.1.25)

For manuscripts utilizing custom algorithms or software that are central to the research but not yet described in published literature, software must be made available to editors and reviewers. We strongly encourage code deposition in a community repository (e.g. GitHub). See the Nature Portfolio guidelines for submitting code & software for further information.

Data

Policy information about availability of data

All manuscripts must include a data availability statement. This statement should provide the following information, where applicable:

- Accession codes, unique identifiers, or web links for publicly available datasets
- A description of any restrictions on data availability
- For clinical datasets or third party data, please ensure that the statement adheres to our policy

The atomic coordinates and all related data of ASK1-D3 mutant structure were deposited in the Protein Data Bank with accession code 7SA1 (PDB:7SA1). All other materials are available from the corresponding author upon request.

Field-specific reporting

Please select the one below that is the best fit for your research. If you are not sure, read the appropriate sections before making your selection.

☒ Life sciences ☐ Behavioural & social sciences ☐ Ecological, evolutionary & environmental sciences

For a reference copy of the document with all sections, see nature.com/documents/nr-reporting-summary-flat.pdf

Life sciences study design

All studies must disclose on these points even when the disclosure is negative.

Sample size	No sample-size calculations were performed; For figures 2,3 and 6 phenotypic analyses, at list 10 plants of each genotype were analyzed for axillary branching quantification and at list 20 seedlings were analyzed for hypothetical assay, as indicated in the manuscript. Sample size (number of plants used for each analysis) was mainly determined by the limitations of our growth chambers. Neverthless they had been proven sufficient to provide robust and significant differences (with very low P values) in reproducible experiments. These numbers are also similar to those classically used by other research groups in other published work with satisfactory results.
Data exclusions	No data were excluded
Replication	Each experiment was reproduced and repeated at least three times.
Randomization	For all studies, individual plants of different genotypes were randomized in the growth chambers to avoid environmental effects.
Blinding	No blinding was performed in the experiments as the control and experiment plants are very different phenotypically and impossible to mistake for each other

Reporting for specific materials, systems and methods

We require information from authors about some types of materials, experimental systems and methods used in many studies. Here, indicate whether each material, system or method listed is relevant to your study. If you are not sure if a list item applies to your research, read the appropriate section before selecting a response.

Materials & experimental systems

n/a	Involved in the study
☐	☒ Antibodies
☐	☒ Eukaryotic cell lines
☒	☐ Palaeontology and archaeology
☒	☐ Animals and other organisms
☒	☐ Human research participants
☒	☐ Clinical data
☒	☐ Dual use research of concern

Methods

n/a	Involved in the study
☒	☐ ChIP-seq
☒	☐ Flow cytometry
☒	☐ MRI-based neuroimaging

Antibodies

Antibodies used	Antibodies were used for Western-Blotting: Monoclonal anti-ubiquitin antibody (Fisher scientific, clone eBioP4D1 (p4D1)antibody produced in mouse) Monoclonal anti-His (Invitrogen MA1-21315, clone His. H8, antibody produced in mouse) Polyclonal anti-GST (Thermo Scientific, Lot CAB4169, antibody produced in rabbit Amersham ECL Mouse IgG, HRP-linked whole Ab (from sheep) Lot 9793520 Amersham ECL Rabbit IgG, HRP-linked whole Ab (from donkey) Lot 12219044
Validation	The monoclonal anti-ubiquitin antibody was tested by immunblotting of treated cell lines, and reported for use in immunoprecipitation, immunoblotting (WB), and immunohistochemical staining on the manufacture website: https://www.thermofisher.com/antibody/product/Ubiquitin-Antibody-clone-eBioP4D1-P4D1-Monoclonal/14-6078-82 The monoclonal anti-His antibody were validate for Western Blot as reported on the manufacture website: https://www.thermofisher.com/antibody/product/6x-His-Tag-Antibody-clone-HIS-H8-Monoclonal/MA1-21315 The polyclonal anti-GST were validate for Western Blot as reported on the manufacture website: https://www.thermofisher.com/antibody/product/GST-Tag-Antibody-Polyclonal/CAB4169

Eukaryotic cell lines

Policy information about cell lines

Cell line source(s)	Expression Systems Sf9 insect cell line, a clonal isolate derived from the parental Spodoptera frugiperda cell line IPLB-Sf-21-AE. Expression Systems Tni (Hi5) insect cell line, derived from ovarian cells isolated from Trichoplusia ni.
Authentication	Cells have been authenticated by the vendors. No further authentication was performed for commercially available cell lines.
Mycoplasma contamination	Cells were not tested for mycoplasma contamination.
Commonly misidentified lines (See ICLAC register)	No commonly misidentified cell lines were used in the study,